arXiv:1206.5575v1 [astro-ph.CO] 25 Jun 2012

Multi-wavelength Observations of the Enduring Type IIn Supernovae 2005ip and 2006jd[1]

Maximilian Stritzinger[2,3], Francesco Taddia[3], Claes Fransson[3], Ori D. Fox[4], Nidia Morrell[5], M. M. Phillips[5], Jesper Sollerman[3], J. P. Anderson[6], Luis Boldt[7], Peter J. Brown[8], Abdo Campillay[5], Sergio Castellon[5], Carlos Contreras[5], Gastón Folatelli[9], S. M. Habergham[10], Mario Hamuy[6], Jens Hjorth[11], Phil A. James[10], Wojtek Krzeminski[5], Seppo Mattila[12], Sven E. Persson[13], Miguel Roth[5]

ABSTRACT

We present an observational study of the Type IIn supernovae (SNe IIn) 2005ip and 2006jd. Broad-band UV, optical and near-IR photometry, and visual-

---

[1] This paper includes data gathered with the 6.5-m Magellan Telescopes, located at Las Campanas Observatory, Chile; the Gemini-North Telescope, Mauna Kea, USA (Gemini Program GN-2010B−Q−67, PI: Stritzinger); the ESO NTT, La Silla, Chile (Program 076.A-0156 and 078.D-0048, PI: Hamuy); and the INT and the NOT (Proposal number 45−004, PI: Taddia), La Palma, Spain.

[2] Department of Physics and Astronomy, Aarhus University, Ny Munkegade 120, DK-8000 Aarhus C, Denmark.

[3] The Oskar Klein Centre, Department of Astronomy, Stockholm University, AlbaNova, 10691 Stockholm, Sweden.

[4] Astrophysics Science Division, Observational Cosmology Laboratory, NASA Goddard Space Flight Center, Greenbelt, MD 20771, USA.

[5] Carnegie Observatories, Las Campanas Observatory, Casilla 601, La Serena, Chile.

[6] Departamento de Astronomia, Universidad de Chile, Casilla 36D, Santiago, Chile.

[7] Argelander Institut für Astronomie, Universität Bonn, Auf dem Hügel 71, D-53111 Bonn, Germany.

[8] Mitchell Institute for Fundamental Physics & Astronomy, Department of Physics & Astronomy, Texas A&M University, College Station, TX 77843, USA.

[9] Institute for the Physics and Mathematics of the Universe (IPMU), University of Tokyo, 5-1-5 Kashiwanoha, Kashiwa, Chiba 277-8583, Japan.

[10] Astrophysics Research Institute, Liverpool John Moores University, Twelve Quays House, Egerton Wharf, Birkenhead CH41 1LD, UK.

[11] Dark Cosmology Centre, Niels Bohr Institute, University of Copenhagen, Juliane Maries Vej 30, 2100 Copenhagen Ø, Denmark.

[12] Tuorla Observatory, University of Turku, Väisäläntie 20, FI-21500 Piikkiö, Finland.

[13] Observatories of the Carnegie Institution for Science, 813 Santa Barbara St., Pasadena, CA 91101, USA.

wavelength spectroscopy of SN 2005ip complement and extend upon published observations to 6.5 years past discovery. Our observations of SN 2006jd extend from UV to mid-infrared wavelengths, and like SN 2005ip, are compared to reported X-ray measurements to understand the nature of the progenitor. Both objects display a number of similarities with the 1988Z-like subclass of SN IIn including: (i) remarkably similar early- and late-phase optical spectra, (ii) a variety of high ionization coronal lines, (iii) long-duration optical and near-IR emission and, (iv) evidence of cold and warm dust components. However, diversity is apparent including an unprecedented late-time r-band excess in SN 2006jd. The observed differences are attributed to differences between the mass-loss history of the progenitor stars. We conclude that the progenitor of SN 2006jd likely experienced a significant mass-loss event during its pre-SN evolution akin to the great 19th century eruption of η Carinae. Contrarily, as advocated by Smith et al. (2009), we find the circumstellar environment of SN 2005ip to be more consistent with a clumpy wind progenitor.

Subject headings: circumstellar matter – supernovae: general – supernovae: individual: SN 2005ip and SN 2006jd – dust, dust formation.

1. INTRODUCTION

Type IIn supernovae (SNe IIn) are thought to originate from the core-collapse of massive stars enshrouded in hydrogen-rich circumstellar material (CSM). Members of this SN class display a variety of photometric and spectral properties, however each member shares the commonality of conspicuous narrow Balmer emission lines (Schlegel 1990; Kiewe et al. 2012).[1] Hα emission typically dominates the spectrum and often exhibits multiple components characterized by a narrow core ($v_{\mathrm{FWHM}} \sim 200$ to 500 km s^{-1}), an intermediate component (v_{FWHM} $\sim$ 2000 to 5000 km s^{-1}), and a broad component ($v_{\mathrm{FWHM}} \gtrsim 10^4$ km s^{-1}). Depending on the nature of the CSM and the dynamics of the explosion, these SNe can be observed from X-ray to radio wavelengths, and often display an infrared (IR) excess attributed to the reprocessing of energy by pre-existing dust, newly-formed dust, or a combination of the two (e.g. Gerardy et al. 2002; Fox et al. 2009). The various observational characteristics of this SN class are therefore modulated by the SN emission, the mass-loss history of the progenitor star, and the physics of the SN–CSM interaction (e.g. Chevalier & Irwin 2011, 2012).

---

[1] Narrow circumstellar lines have also been identified in some Type IIL SNe, e.g. SN 1979C (Branch et al. 1981), as well as in the SN 1984E in NGC 3169 (Dopita et al. 1984; Henry & Branch 1987).

Observations have now led to an emergent picture of a number of broadly different types of SNe IIn. At the top of the luminosity scale are the exceedingly bright ($M_V \sim -22$ mag) objects, including amongst others; SN 2005ap (Quimby et al. 2007), SN 2006gy (Ofek et al. 2007; Smith et al. 2007; Woosley, Blinnikov, & Heger 2007; Smith & McCray 2007; Agnoletto et al. 2009), SN 2006tf (Smith et al. 2008), SN 2008am (Chatzopoulos et al. 2011) and SN 2008iy (Miller et al. 2010). The exact nature of these objects is a matter of debate, but the general consensus seems to require one or more dense shells of CSM ejected from the progenitor during sequential luminous blue variable (LBV)-like eruptions in the decades prior to explosion. Lower on the luminosity scale ($M_V \sim -17$ to -19 mag) are the 1988Z-like SNe IIn (Turatto et al. 1993; Pastorello et al. 2002), which are thought to be powered for years by X-ray emission generated by the SN blast wave interacting with either a highly asymmetric distribution of CSM or a clumpy-wind circumstellar medium (e.g. Chugai & Danziger 1994; Fransson et al. 2002). Thirdly, are the 1994W-like SNe IIn (Sollerman, Cumming, & Lundqvist 1998; Kankare et al. 2012) that reach moderate peak brightnesses ($M_V \sim -18$ mag), and whose light curves exhibit a $\sim$ 100 day long plateau phase followed by a sharp drop in luminosity. The origin of the 1994W-like objects is an open question with possibilities ranging from low-luminosity SNe interacting with CSM (Chugai et al. 2004), to colliding shells of material (Dessart et al. 2009). In addition to these groups there appears to be a variety of other SNe that interact with their CSM, ranging from amongst others, SN 1997cy which was suggested to be linked to a gamma-ray burst (Germany et al. 2000; Turatto et al. 2000), to 2002ic-like SNe that may or may not be associated with white dwarf progenitors (see e.g. Hamuy et al. 2003; Deng et al. 2004; Benetti et al. 2006, and references therein). Clearly, a diverse set of progenitor scenarios are required to plausibly explain the various objects classified under the SN IIn designation.

SN 2005ip appeared as a 1988Z-like object whose SN–CSM interaction powered its spectral energy distribution (SED) for the duration of years, and led to the formation of a rich forest of coronal lines observed over all epochs. These coronal lines have been seen in only a handful of SNe IIn, e.g., SN 1988Z (Turatto et al. 1993), SN 1995N (Fransson et al. 2002), SN 1997ef (Hoffman et al. 2008), as well as in the Type II SN 1987A (Gröningsson et al. 2006), however in the case of SN 2005ip their early appearance, high-ionization and long duration was unprecedented (Smith et al. 2009). Such coronal lines may be formed from the photoionization of dense gas by X rays produced from shocks, or as in the case of SN 1987A, hot gas with plasma temperatures in excess of $\sim 10^6$ K (Gröningsson et al. 2006).

Previous studies of SN 2005ip have documented its observational properties; however, differences of opinion are found in the literature regarding the exact nature of the progenitor, and details of the dust emission (Smith et al. 2009; Fox et al. 2009, 2010). Based on their circumstellar (CS) wind speed and dust mass estimations, Fox et al. (2010) have argued the progenitor was a LBV star. Alternatively, Smith et al. (2009) suggest the progenitor was akin to a red supergiant (RSG) star –like VY Canis Majoris (VY CMa) (e.g. Chugai & Danziger 1994; Fransson et al. 2002; Smith et al. 2009)– that exploded in the midst of (or soon after) a period of enhanced mass-loss characterized by eruptive mass ejections. In this instance the mass-loss mechanism might be linked to pulsation-driven super-winds (Heger et al. 1997; Yoon & Cantiello 2010).

In this paper we present UltraViolet (UV), optical and near-IR photometry, and visual-wavelength spectroscopy of SN 2005ip obtained over the course of the *Carnegie Supernova Project* (CSP; Hamuy et al. 2006). These observations complement the already existing dataset, and are used to interpret a related object, SN 2006jd. Our observations of SN 2006jd cover UV, optical and IR wavelengths, and are combined with reported X-ray (Chandra et al. 2012) and mid-IR measurements (Fox et al. 2011) to gain insight on the progenitor star, its mass-loss history, and details concerning the interaction of the (subsequent) SN with the circumstellar environment. The organization of this paper is as follows. Section 2 contains a description of the observations obtained for both objects, Section 3 presents the final photometry and spectroscopic sequences, and an analysis concerning the dust emission, Section 4 contains the discussion, and this is followed by our conclusions in Section 5.

2. OBSERVATIONS

2.1. Supernova 2005ip

SN 2005ip was discovered on 5.2 November 2005 UT (Boles et al. 2005) in the Scd galaxy NGC 2906 (see Figure 1). With J2000.0 coordinates of $\alpha = 09^{\mathrm{h}}32^{\mathrm{m}}06\overset{\mathrm{s}}{.}42$ and $\delta = +08^{\circ}26'44\overset{''}{.}4$, this SN was located $2\overset{''}{.}8$ E and $14\overset{''}{.}2$ N of the center of the host. From previous non-detection images obtained on 21 January 2005 no precise constraints can be placed on the explosion epoch, however, from a black-body (BB) fit to their earliest spectrum, Smith et al. (2009) claimed the explosion epoch to have occurred 8–10 days prior to discovery. In what follows we present our data with respect to the date of discovery, i.e. JD = 2453679.66. According to the IR dust maps of Schlegel, Finkbeiner & Davis (1998), the Galactic color excess in the direction of SN 2005ip is $E(B-V)_{\mathrm{MW}} = 0.047$ mag. The spectroscopic observations presented below show no signs of Na I D absorption at the redshift of the host galaxy, indicating negligible host galaxy extinction. We therefore assume the total color excess to be solely attributed to Galactic reddening, which for a standard $R_V = 3.1$, yields a visual extinction of $A_V = 0.15$ mag. NED lists the host recession velocity as 2140 ± 6 km s^{-1}. Correcting for Virgo, Great Attractor and Shapley infall models, and assuming the WMAP five-year cosmological parameters of $\mathrm{H}_0 = 70.5$ km s^{-1} Mpc^{-1}, $\Omega_m = 0.27$ and $\Omega_\Lambda = 0.73$, we obtain a luminosity distance to the host galaxy of 34.9 ± 0.6 Mpc.

Smith et al. (2009) published optical spectroscopy and an unfiltered light curve of SN 2005ip extending ~ 4 years. These observations were later complemented with near-IR and *Spitzer* mid-IR photometry and spectrophotometry by Fox et al. (2009, 2010). Here we present CSP optical ($uBgVri$) and near-IR (YJH) light curves of SN 2005ip. Our photometric monitoring began four days after discovery, and extend 5.3 years, with the last near-IR observations obtained on 21.1 February 2011 UT.

The majority of our imaging of SN 2005ip (and SN 2006jd) was obtained at the Las Campanas Observatory (LCO) with the Henrietta Swope 1.0 m telescope equipped with both a direct optical camera named after its detector "SITe3", and the near-IR imaging camera called "RetroCam". These data are accompanied with additional imaging taken with the Irénée du Pont 2.5 m telescope. Optical du Pont images were obtained with the direct CCD camera known as "Tek 5", while near-IR images were taken with the Wide-field InfraRed camera called "WIRC"; see Hamuy et al. (2006) for details regarding these instruments.

An in-depth description of CSP observational procedures, data reduction techniques, and the computation of definitive photometry in the *natural* photometric system is described in Contreras et al. (2010, C10). The only difference with respect to the photometry published by C10 and here, is that no host galaxy template subtraction has been performed on the science images of SNe 2005ip and 2006jd. This is simply because these SNe are still visible in deep images taken with the du Pont telescope. However, in the future when useful template images are obtained, an updated version of the photometry will be placed on the CSP webpage.[2]

SN photometry is computed differentially with respect to a local sequence of stars. Absolute photometry of the optical and near-IR local sequence of SN 2005ip was determined relative to photometric standard stars observed over the course of 6 and (a minimum of) 9 photometric nights, respectively. The position of each local sequence star and their calibrated magnitudes are listed in Table 1. The averaged optical magnitudes are on the Smith et al. (2002) $u'g'r'i'$ and Landolt (1992) BV photometric systems, while the near-IR magnitudes are on the Persson et al. (1998) JHK_s photometric system. Y-band photometry of the local sequence is calibrated relative to the $(J - K_s)$ color relation given in Hamuy et al. (2006, see their Appendix C, equation C2).

Limited follow up imaging of SN 2005ip was conducted from space with the UltraViolet

---

[2] Electronic files of SNe 2005ip and 2006jd in `ASCII` format are available on the CSP webpage `http://obs.carnegiescience.edu/CSP/data` .

Optical Telescope (UVOT) aboard the *Swift* satellite (Roming et al. 2005). Four epochs of $[uvw2][uvm2][uvw1]$-band photometry were obtained covering the flux evolution from day 146 to 1154, while an additional epoch on day 2012 was taken with the $[uvw1]$ filter.[3] Aperture photometry was computed from the UVOT images following the method described by Brown et al. (2009), but updated to the zero-points of Breeveld et al. (2011). As this SN (and SN 2006jd, see below) has not faded completely in several followup observations, we utilize a background region with a flux level similar to that near the SN position rather than utilizing the standard galaxy-subtraction technique.

The final UV, optical and near-IR light curves of SN 2005ip are plotted in Figure 2. The corresponding optical and near-IR photometry in the natural system are listed in Tables 2 and 3, while the UVOT photometry is given in Table 4.

In addition to the photometric follow up, 13 epochs of low-resolution visual-wavelength spectroscopy of SN 2005ip covering the first five and a half months (23 November 2005 – 23 April 2006) of evolution was obtained with an assortment of telescopes at LCO and the La Silla Observatory. Two very late spectra were also obtained 1844 and 2352 days past discovery with the 2.5 m Isaac Newton Telescope and the 2.5 m Nordic Optical Telescope, from which we are able to measure emission features (e.g. Hα) associated with post-shock gas. Each spectrum was reduced in the standard manner using IRAF[4] scripts following the techniques described in Hamuy et al. (2006). When necessary the fluxing of the spectra was adjusted to match what was obtained from the broad-band photometry. The journal of spectroscopic observations is given in Table 5, and 8 of the 15 epochs of spectra are plotted in Figure 3.

2.2. Supernova 2006jd

SN 2006jd was discovered on 12.5 October 2006 UT in the SBb galaxy UGC 4179 by the Lick Observatory Supernova Search (LOSS; Prasad & Li 2006). With J2000.0 coordinates of $\alpha = 08^{\rm h}02^{\rm m}07\overset{\rm s}{.}43$ and $\delta = +00^\circ 48' 31\overset{''}{.}5$, SN 2006jd is located $22\overset{''}{.}0$ E and $1\overset{''}{.}3$ S from the center of the host galaxy. A V-band image of the galaxy with the SN indicated is shown in Figure 4. The previous LOSS non-detection on 21.2 April 2006 UT precludes a precise estimation of

---

[3] The central wavelengths and FWHM values of the UVOT filters are as follows: $[uvw2]$ ($\lambda_c = 1928$ Å; FWHM = 657 Å), $[uvm2]$ ($\lambda_c = 2246$ Å; FWHM = 498 Å), and $[uvw1]$ ($\lambda_c = 2600$ Å; FWHM = 693 Å).

[4] IRAF is distributed by the National Optical Astronomy Observatories, which are operated by the Association of Universities for Research in Astronomy, Inc., under cooperative agreement with the National Science Foundation.

the explosion epoch. In the remainder of the paper the observations of SN 2006jd will be presented with respect to date of discovery, i.e. JD = 2454021.04. Initially classified as a Type IIb event (Blondin et al. 2006), it was later re-designated by Immler et al. (2007) as a Type IIn SN. The Galactic color excess in the direction of UGC 4179 is listed in NED to be $E(B-V)_{\rm MW} = 0.054$ mag. Under close inspection of our spectroscopic sequence we find no indication of Na I D absorption at the redshift of the host galaxy, suggesting the SN suffered little to no host extinction. In what follows the total color excess is assumed to be only due to Galactic reddening. Adopting a standard reddening law characterized by an $R_V = 3.1$ then implies a visual extinction in the direction of SN 2006jd to be $A_V = 0.18$ mag. NED lists a recession velocity for UGC 4179 of 5563 ± 5 km $\rm s^{-1}$, which when corrected for the 3-component Virgo, GA and Shapley infall model, and assuming the standard five-year WMAP cosmological parameters, corresponds to a luminosity distance of 83.8 ± 1.5 Mpc.

Our photometric observations commenced a week after discovery and extend over a duration of nearly four and a half years. The local sequence of stars used to compute photometry was calibrated with respect to standard field observations obtained on 11 nights in the optical and, depending on the specific star, between 3 and 22 nights in the near-IR. The local sequence is given in Table 1. Final optical and near-IR photometry of SN 2006jd is given in Tables 6 and 7, respectively. The corresponding light curves are plotted in Figure 5.

Limited follow up imaging of SN 2006jd was also performed with *Swift*. Seven epochs of $[uvw2][uvm2][uvw1]$-band photometry were obtained covering the flux evolution from day 401 to 790. The final UVOT photometry is listed in Table 4, and plotted in Figure 5.

We also obtained an epoch of mid-IR imaging with IRAC (InfraRed Array Camera) aboard *Spitzer*. Two channels of imaging were taken at 3.6 μm and 4.5 μm on 22 June 2011 or 1713.8 days past discovery. PSF photometry of the SN implies flux values of $1.53 \pm 0.01 \times 10^{-17}$ erg $\rm cm^{-2}$ $\rm s^{-1}$ $\rm Å^{-1}$ at 3.6 μm and $1.59 \pm 0.01 \times 10^{-17}$ erg $\rm cm^{-2}$ $\rm s^{-1}$ $\rm Å^{-1}$ at 4.5 μm. These values are $\sim 30\%$ of those measured previously in images taken on day $\sim$ 1150, and are qualitatively in agreement with the slow decline of the K_s-band light curve (see below). In what follows the *Swift* and *Spitzer* observations are combined with optical and near-IR photometry, and measurements of the X-ray and radio flux to construct a nearly complete SED at day $\sim$ 1638.

Seventeen epochs of low-resolution, long-slit visual-wavelength spectroscopy of SN 2006jd were obtained with an assortment of telescopes at LCO, and the La Silla and Mauna Kea Observatories (see Table 5). These spectra were also reduced in a standard manner, and their fluxing was adjusted to match that derived from the broad-band photometry. The spectroscopic sequence covers all phases of the flux evolution, beginning 2 weeks from discovery to 39 months later. To highlight the rich structure contained within these spectra a subset of the full spectroscopic series is shown in Figure 6.

3. RESULTS

3.1. Host Galaxy Metallicity

Here metallicities in the vicinity of SNe 2005ip and 2006jd are derived using emission line diagnostics. To do so for SN 2005ip we extracted from the 2-D spectrum obtained on day 1844 emission from an H II region which lies close to the position of the SN. Inspection of the 1-D spectrum revealed Hα and [N II] $\lambda\lambda$6548, 6583 emission lines from which Gaussian fits provide flux measurements that imply a local metallicity of 12+log(O/H)=8.73 ± 0.18 dex calibrated on the N2 scale of Pettini & Pagel (2004).

The metallicity of the environment of SN 2006jd was also measured in a similar fashion. By extracting from the 2-D spectrum taken on day 423 a series of H II regions in close proximity to the SN, the resultant emission lines imply a N2 calibrated metallicity of 12+log(O/H)=8.28 ± 0.18 dex. For comparison, using the [N II]/[O II] diagnostic (Kewley & Dopita 2002) the series of H2 regions provide metallicity estimates in the range of $8.60 < 12+\log(\mathrm{O/H}) < 8.75$ dex.

In summary we find the local environments of SN 2005ip to be comparable with the known solar metallicity of ~ 8.69 dex (Asplund et al. 2009), while depending on the specific emission line diagnostic, the environment of SN 2006jd lies within the range between that of the LMC to solar.

3.2. Light Curves

3.2.1. Supernova 2005ip

The majority of our optical and near-IR photometry plotted in Figure 2 follow the initial ~ 200 days of evolution, while several additional epochs extend to day 1565 (optical) and day 1934 (near-IR). In addition to our own photometry, included as filled squares in Figure 2 are the unfiltered (Smith et al. 2009) and near-IR (Fox et al. 2009) light curves taken from the literature. In general there is excellent agreement between the datasets.

Initially, the overall flux evolution is characterized by a rapid, linear decline (in magnitude) over the first ~ 55 days. Subsequently, the slope of the decline further increases in the optical bands, while simultaneously, the H- and K_s-band light curves show an increase of emission. This is highlighted in the inset of Figure 2, where the vertical dashed line indicates the epoch (day 55) when these transitions occur. As discussed in Section 3.4, these phenomena are believed to result from the *in situ* formation of dust within a cold, dense shell (CDS) of gas that lies between the forward and reverse shock produced by SN–CSM interaction. If the newly formed dust was distributed homogeneously in a spherical shell one would expect the bluest optical bands to be attenuated more significantly then those in the red, which is what we observe when comparing the slopes of the light curves derived before dust formed to what is measured post dust formation.

From day 100 to 150 the u- to J-band light curves continue to decline in brightness, at which point a break occurs post day 150, followed by a long-duration plateau phase. This is best illustrated by the r-band light curve, which reveals the plateau phase extending beyond day 1500. Contrarily, from the onset of dust formation the H and K_s light curves brighten ≈ 0.2 mag over a 5 week period, and subsequently, settle onto a slow linear decline phase lasting over the duration of our observations.

Finally, the UV light curves appear to follow, similar to the redder wavelengths, a plateau phase characterized by nearly constant emission between $\sim$ day 500 to day 1000, whereupon they appear to turn over and slowly decline in flux over time.

3.2.2. Supernova 2006jd

The light curves of SN 2006jd displayed in Figure 5 reveal a rich evolution that in some ways resembles SN 2005ip. Over the first ~ 150 days the $ugriBVY$-band light curves decline in a linear fashion with slopes of $\lesssim 0.01$ mag per day. Subsequently, an abrupt break occurs marking the onset of a plateau phase which lasts $\gtrsim 500$ days. Most interestingly, over this time the r-band light curve reveals an unprecedented evolution characterized by an excess of flux that peaks on day 544 at ≈ 1.0 mag above its brightness measured during the start of the plateau phase. As shown later, this excess of flux is attributed to a significant increase in Hα emission (see Figure 14) as the SN blast wave interacts with a dense shell of material (see Section 4.2). Following the plateau phase that ends some ~ 750 days past discovery, the optical light curves evolve along a slow, linear (~ 0.001 mag per day) decline phase through the end of our observations which conclude on day 1638.

On the other hand, from the commencement of our observations the near-IR JHK_s light curves exhibit an increase in flux which peaks on day ~ 40. Subsequently, an extended period of constant emission ensues, and then > 500 days later the light curves settle along a slow, linear decline (~ 0.002 mag per day), which we follow until day 1593.

Also plotted in Figure 5 are the *Swift* UVOT $[uvw2][uvm2][uvw1]$-band light curves. Beginning on day 401, the UVOT observations cover 7 epochs extending over a duration of 389 days, and indicate that the UV emission, like the optical and near-IR light emission, was also relatively constant during this time period.

3.3. SEDs and Quasi-Bolometric Light Curves

In order to estimate the physical parameters, i.e. temperature, radius and luminosity of the underlying emitting regions, the available broad-band observations are used to construct SEDs. BB fits to the resulting optical and IR SEDs then provide an avenue to constrain these parameters, as well as to place lower limits on the bolometric luminosity, and as we discuss later, provide dust mass estimates.

To construct comprehensive SEDs the near-IR light curves were first interpolated following the method of Pastorello et al. (2009, see their Section 3) so magnitude estimates could be made for those epochs in which optical photometry was obtained. Next the optical/near-IR photometry was corrected for reddening using the $E(B-V)_{tot}$ color excess values discussed in Section 2, and the standard Cardelli, Clayton, & Mathis (1989) extinction curve characterized by $R_V = 3.1$. The extinction-corrected optical and near-IR photometry was then converted to flux at the effective wavelength of each bandpass. The resulting SEDs of SNe 2005ip and 2006jd at a selection of six epochs covering each main phase of flux evolution are plotted in Figure 7. The inset in each panel of Figure 7 indicates the corresponding phases with regard to the light curve.

We next proceed to fit each SED simultaneously with a two-component BB function in the form of

$$F_\lambda(T_{h,w}, R_{h,w}) = \frac{2\pi hc^2}{D^2\lambda^5}\left(\frac{R_h^2}{e^{(hc/\lambda kT_h)}-1} + \frac{R_w^2}{e^{(hc/\lambda kT_w)}-1}\right). \tag{1}$$

Here c, h and k are the standard symbols for their respective fundamental constants, $T_{h,w}$ and $R_{h,w}$ correspond to the temperature and radius of each Planck $BB_{h,w}$ component, and D is the distance to the underlying SN. The first term in Equation 1 corresponds to a 'hot' BB_h component and is derived from fits to the $uBgVi$-band flux points, while the second term corresponds to a 'warm' BB_w component derived from fits to the HK_s-band flux points. These components represent different emitting regions, with the former being coupled to the SN ejecta, and the latter to mostly warm, thermal dust emission. To obtain reasonably accurate $BB_{h,w}$ fits to the SEDs it proved necessary to exclude the rYJ-band flux points as their associated bandpasses include prevalent emission lines of Hα, He I $\lambda10380$ and Pβ $\lambda12830$, respectively. The resulting best-fit combined $BB_{h,w}$ functions are over-plotted on the SEDs in Figure 7 as solid lines. Note that for presentation clarity the Rayleigh-Jeans tail of the BB_w component is not included in the figure.

The resulting values of $T_{h,w}$, $L_{h,w}$ and $R_{h,w}$ computed from the $BB_{h,w}$ fits shown in Figure 7 are given in Table 8, as well as the ratio of L_h to $L_h + L_w$. The corresponding values of $T_{h,w}$, $L_{h,w}$ and $R_{h,w}$ computed from fits to SEDs constructed from our full series of observations are plotted in Figure 8. Also shown in the bottom panel is the ratio of L_w to $L_h + L_w$. Under close inspection, Figure 7 reveals that the SED of both objects exhibit similar characteristics at each of their main evolutionary phases. At the earliest epochs the vast majority of flux is emitted at optical wavelengths. However, by day $\gtrsim 100$ the optical portion of the SED accounts for only half of the total optical+near-IR emission, and over time continues to decline, while simultaneously the near-IR emission exhibits an excess that by day ~ 200 dominates the optical+near-IR spectrum (see last column of Table 8). The prevalent increase and long-duration of the near-IR excess signifies enhanced thermal emission from warm dust (Fox et al. 2009). Interestingly, both objects also have nearly identical values of $T_w \sim 1500$ K at the time when newly formed dust is thought to condense, while this warm dust component appears to be more luminous and extends to further distances in SN 2006jd (see Section 4.3 for further discussion).

To compute quasi-bolometric light curves of SNe 2005ip and 2006jd we take the approach of summing the luminosities derived from the two-component $BB_{h,w}$ fits with the flux contained within the emission lines covered by the rYJ-bands (i.e. the flux contained under the dashed line plotted in Figure 11, see below). The resulting quasi-bolometric light curves are shown in Figure 9 as points. Also included in this figure are the individual BB_h (dashed lines) and BB_w (dotted lines) components, and the summation of these two components (solid lines). We note that our quasi-bolometric light curves provide only a lower limit to the total flux as they neglect emission associated with wavelength regimes not sampled by our photometry, including emission from X-ray to UV wavelengths and from mid-IR to radio wavelengths. Nevertheless, the Rayleigh-Jeans tail associated with the BB_w component *does* account for a portion of thermal emission that lies beyond the K_s band, and indeed this flux is a dominant source of the quasi-bolometric light curves from day ~ 100 and beyond (see dotted lines). Note that the BB_w component provides a major part of the total optical+near-IR SED from the onset of the plateau phase and beyond. This long-lasting emission implies that the quasi-bolometric light curve is powered more by SN–CSM interaction rather than radioactive decay.

Comparing the bolometric light curves of SNe 2005ip and 2006jd, we find that at the earliest epochs they exhibit similar peak luminosity of roughly $\sim 3.2{\times}10^{42}$ erg s^{-1}, which is equivalent to an absolute bolometric magnitude of ~ -17.6. Later as each object evolves to the mid-points of their respective plateau phase, Figure 9 indicates SN 2006jd clearly outshines SN 2005ip, reaching a maximum difference in luminosity of $\sim$ 0.7 dex or about $\sim$ 1.7 mag (see also middle panel of Figure 8). This excess of IR flux observed in SN 2006jd suggests that it has a larger amount of dust. To see if this is indeed the case, we proceed to estimate the dust mass associated with these two SNe.

3.4. Dust Emission and Mass Estimates

Near-IR observations of SNe 2005ip and 2006jd provide compelling evidence for the presence of a warm ($T_w \sim 1500$ K) dust component. The ever increasing near-IR emission at early phases supports the notion of warm dust condensation. This emission dominates the SED within $\sim$ 100 days past discovery and continues to do so for the duration of hundreds of days. The long-duration of the near-IR excess is best explained by a dust heating mechanism associated with radiative shocks formed at the interface of the SN–CSM interaction (see Fox et al. 2009, for a detailed discussion). Interestingly, the turn-on of the near-IR excess coincides in time with an ever increasing attenuation of the red wing of the Hα profile (see below), and in the case of SN 2005ip, a steepening decline in the optical band light curves (see Figure 2). Such phenomena are usually attributed to dust condensation within either the fast SN ejecta or in the CDS of post-shock gas lying between the interface of the forward and reverse shocks. Dust forming in either of these regions preferentially scatters and absorbs photons emitted from the far side of the ejecta and thereby causes the attenuation of the red wing of prevalent emission profiles, and can lead to steeper decline rates for the blue light curves. Alternatively, the increased attenuation of the red side of the line profile might, in some cases, be related to an optical depth effect (see Section 4.3 and Smith et al. 2012).

In Figure 10 the evolution of the Hα emission profile of both SNe 2005ip and 2006jd over the first four months of observations is plotted. The ever increasing attenuation of the red side of Hα clearly occurred in both objects. This behavior was already noted in SN 2005ip (Smith et al. 2009), however for SN 2006jd, Fox et al. (2011) argued there was no evidence for such a phenomenon.[5] Clearly, SN 2006jd also exhibits an increased attenuation of red flux at early times.

---

[5] Fox et al. (2011) based this claim on the comparison of spectra obtained on day 395 and 564. Given that the effects of newly formed dust are greatest *at early times* it is of no great surprise they did not observe this behavior. This highlights the necessity of early phase spectroscopy to identify signatures of newly formed dust.

In addition to the possibility that warm dust formed at early times, Fox et al. (2010, 2011) determined from *Spitzer* mid-IR imaging that both SNe 2005ip and 2006jd exhibit thermal emission associated with a cold dust component ($T_c \sim 600$ K). These authors attribute this emission to pre-existing dust, which is illuminated by photons that ultimately originate from radiative shocks produced from the SN–CSM interaction.

We now endeavor to estimate the dust mass associated with the warm near-IR and cold mid-IR dust components. To estimate the mass (M_d) of each of these components in SNe 2005ip and 2006jd we follow the prescription of Fox et al. (2010, and references therein), which entails fitting the SEDs with the following expression

$$F(\lambda) = \frac{M_d B_\lambda(T_d) \kappa_\lambda(a)}{D^2}. \quad (2)$$

This formalism is valid for small optical depths, and allows us to directly constrain M_d. Here $B_\lambda(T_d)$ is the Planck BB function, $\kappa_\lambda(a)$ is the dust mass absorption coefficient for a dust particle with radius, a, and D is the distance to the emitting source. In the following we adopt the $\kappa_\lambda(a)$ functions of Fox et al. (2010, see their Figure 4) for a dust composition consisting of graphite grains with radii $a = 0.01$ μm, 0.1 μm, and 1 μm. Based on the absence of the 9.6 μm feature in their *Spitzer* observations, Fox et al. (2010) excluded silicates in their analysis of SN 2005ip. To be consistent, in the follow we compute M_d for both SN assuming that their dust components are composed of only graphite. Equation 2 is commonly used for a wide variety of astrophysical applications, and is based on the assumption that the emitting dust is: (1) dominated by one grain size and (2) emits at a single temperature.

Fitting Equation 2 to the series of SEDs plotted in Figure 7, with, M_d and T_d as free parameters, warm dust mass estimates are obtained for graphite grains with radii of $a = 0.01$ μm, 0.1 μm, and 1 μm. The resulting values for SNe 2005ip and 2006jd are listed in Table 9, and the corresponding best-fit function of Equation 2 for the grain size of radius $a = 0.1$ μm is over-plotted on the SEDs of Figure 7 as dashed lines. Note that the solid BB fits included in this figure correspond to a graphite grain size of radius $a = 1.0$ μm. The results of the various fits give increased dust masses as a function of phase, and are strongly sensitive to the adopted grain size. For the range of dust grain sizes and assuming a 4π covering factor, we obtain limits on M_d ranging from 0.2–$6.0\times10^{-4} M_\odot$ and 0.7–$9.8\times10^{-4} M_\odot$ for SNe 2005ip and 2006jd, respectively.

To place limits on M_d associated with the cold dust component, we turn to *Spitzer* mid-IR observations. Plotted in Figure 11 is the full SED of SN 2005ip (left panel) at day $\sim$ 930 and SN 2006jd (right panel) at day $\sim$ 1638. Here the mid-IR flux points for SN 2005ip are taken from Fox et al. (2010), while for SN 2006jd we interpolated between the mid-IR flux values presented in Fox et al. (2010) and the values derived from our recent *Spitzer* observations. In this way we avoid the uncertainty incurred from large extrapolation of optical and near-IR fluxes to the date of our latest *Spitzer* observation. Also plotted in each panel is a late phase *Hubble Space Telescope* (HST) spectrum of the 1988Z-like SN 1995N (Fransson et al. 2002), scaled to match the ground-based u- and B-band flux points. The HST spectrum suggests that the UV excess exhibited by the UVOT observations is associated with numerous emission lines including, amongst others, [O III], [Si III], Fe II, Mg II, [C III], and [N III] (see Fransson et al. 2002, Fig. 7). Finally, for completeness the inset contained within the plot of SN 2006jd also included reported X-ray and radio measurements (Chandra et al. 2012).

Over-plotted as a black line in each panel of Figure 11 is the sum of a simultaneous three-component BB fit corresponding to a hot, warm and cold component. In both cases the hot BB_h component fit is made to the $uBgVi$ flux points, while the warm BB_w component is fit to the HK_s flux points, and the cold BB_c component is fit to the mid-IR flux points. As mentioned in Section 3.3 the rYJ flux points are not used to constrain the best BB fits due to strong emission lines contained within these passbands. Following Fox et al. (2011), we fit the near- and mid-IR portion of the SED with distinct BB components. This indicates the presence of two discrete dust emitting regions, which are characterized with warm BB_w and cold BB_c temperatures of roughly $\mathrm{T}_w \sim 900$ K and $\mathrm{T}_c \sim$ 500–700 K, respectively.

Plotted as blue lines in Figure 11 are the best-fit cold BB_c components for dust grain size of 0.1 μm, and the corresponding temperatures, radii and dust masses are listed in Table 10. These fits suggest cold masses of $\sim 0.01\ M_{\odot}$ and $\sim 0.02\ M_{\odot}$ for SN 2005ip and 2006jd, respectively. As in the case of fitting the warm dust component, our computed values of M_d for the cold dust are quite sensitive on the composition and size of the dust grains. Finally we note that from the full SEDs we are able to estimate that the flux associated with cold dust component at these late epochs represents $\sim 1\%$ of the total UVOIR flux.

3.5. Optical Spectroscopy

3.5.1. Supernova 2005ip

The spectroscopic sequence of SN 2005ip shown in Figure 3 follows the evolution leading up to the plateau phase, while the last spectrum probes the emission at very late times. A detailed description of the spectral evolution of SN 2005ip is presented by Smith et al. (2009); here we summarize the overall appearance, and use these observations as a comparison to SN 2006jd. The early phase spectra show a significant multi-component Hα emission feature and a broad Ca II $\lambda\lambda$8498, 8542, 8662 bump, superposed on a pseudo-continuum exhibiting an excess of flux bluewards of $\sim$ 5700 Å. Hα dominates the spectrum, and at early phases the Balmer decrement, as measured from the sum of all components is $\approx$ 25. Narrow emission features attributed to [O III] $\lambda\lambda$4959, 5007, He I $\lambda\lambda$5876, 6678, 7065, 7281, [Ar III] λ7136 and [O II] λ7325 are observed both at early- and late-times. A remarkable feature displayed in the spectra of SN 2005ip are the high-ionization coronal emission lines, e.g. [Ar XIV], [Fe XIV] and [Ar X], which are discernible at the earliest epochs, and over time, grow in strength relative to the continuum flux (see Smith et al. 2009, for a detailed analysis of these features). Over the duration of its evolution the majority of emission features remain as narrow lines, however by day 169, He I $\lambda\lambda$5876, 7065 show intermediate-width components, characterized by FWHM velocities of $\sim$ 3500 km s^{-1} and 2500 km s^{-1}, respectively.

A detailed discussion on the evolution of Hα in both SN 2005ip and 2006jd is provided below in Section 3.5.3.

3.5.2. Supernova 2006jd

The optical spectroscopic sequence of SN 2006jd shown in Figure 6 covers 1520 days of evolution. The appearance of these spectra resembles those of SN 1988Z and SN 2005ip (see Section 4.1). At early epochs the spectrum of SN 2006jd contains broad Hα and Ca II $\lambda\lambda$8498, 8542, 8662 emission features, as well as an excess of continuum flux bluewards of $\sim$ 5700 Å. The Hα feature is composed of an intermediate-width component situated on top of a broad, asymmetric component, which shows more flux in the blue wing. Compared to SN 2005ip, the Balmer decrement shown by SN 2006jd, as measured from the sum of components is even more pronounced, ranging from $\approx$ 55 to $\approx$ 40 between the first and last spectra. In addition narrow, weaker lines associated with, amongst others, [Ne III] $\lambda\lambda$3869, 3967, [O III] $\lambda\lambda$4363, 4959, 5007, [N II] λ5755 and He I $\lambda\lambda$4471, 5876, 6678, 7065 are also present. Over time these lines tend to increase in relative strength compared to the continuum, while a number of conspicuous lines from various other ions appear. This is illustrated in Figure 12 where the first (day 22) and last (day 1542) spectra of SN 2006jd are compared, with ions associated with the most prevalent narrow lines labeled, and their corresponding line fluxes are given in Table 11.

From this comparison emission features associated with [O III] $\lambda\lambda$4959, 5007 and He I $\lambda\lambda$5876, 7065 are seen to gain an intermediate-width component. This component is typically associated with either post-shock gas or unshocked ejecta gas photoionized by shock radiation (e.g. Fransson et al. 2002), and here is observed to "turn on" by day 414, and by day 1542 it exhibits FWHM velocities between $\sim$ 1000–1200 km s^{-1}. A close inspection of the day

1542 spectrum of SN 2006jd also reveals various medium- and high-ionization coronal lines, e.g. [Fe VII] $\lambda\lambda$5159, 5276, 5721, 6087, [Fe X] λ6375, [Ar X] λ5535, [Fe X] λ6375 and [Fe XI] λ7892. Hints of these coronal features are evident as small notches in the earliest spectra (see Figure 12), but by late phases, they too have grown considerably in strength relative to the continuum flux. With an ionization potential of 442.3 eV, [Ar X] λ5535 is the highest excitation coronal line identified in SN 2006jd. The overall luminosities of the coronal lines identified in SN 2006jd remain relatively constant over the first $\sim$ 1000 days of evolution, but by the time of the last spectrum, their luminosities appear to drop by a factor of ten. This is shown in Figure 13 which shows the luminosity evolution for the coronal lines, and a number of the prominent forbidden and He I lines.

Provided with the line fluxes given in Table 11, we searched for various line diagnostics to constrain physical parameters associated with the underlying emitting gas. Unfortunately, most of the interesting line ratios are blended with lines of Fe II, however the [O III] $\lambda5007/\lambda4363$ ratio does appear to be free of contamination. Assuming negligible host galaxy reddening, the observed [O III] $\lambda5007/\lambda4363$ ratios measured from the series of spectra imply number densities of $> 10^6$ cm^{-3} in the narrow line region. The fact that these features are observed also implies a minimum gas temperature of 1.0×10^4 K. The implications of this quite high gas density are discussed in relation to the mass-loss history of the progenitor in Section 4.

3.5.3. Evolution of Hα line profiles

Through careful examination of the Hα emission profile and its time-evolution one can gain insight on the dynamics of the SN–CSM interaction, a more complete understanding of the shock physics, and clues concerning the geometry of the CSM. Presented in Figure 14 (left panel SN 2005ip and right panel SN 2006jd) are the full time-series of spectra zoomed in on the position of Hα. Close inspection reveals both broad- and intermediate-width components, and in addition, the early phase spectra also exhibit a hint of a narrow component, which is only partially resolved. Most interestingly, a close comparison of the broad component between the two objects reveals this feature to be highly asymmetric in SN 2006jd from the onset of our observations (see also Figure 10), showing more flux in the blue wing. Possible explanations of this peculiarity could be (i) occultation of the red side of the SN by an optically thick ejecta (see Section 4.3), (ii) an asymmetric explosion, or (iii) fast gas moving through a clumpy ejecta (e.g. Fransson et al. 2002). As a result of this asymmetry, traditional Gaussian fits to the broad-component render unreliable FWHM velocity measurements. We therefore adopted the approach of measuring the blue velocity at zero intensity (BVZI), which is equivalent to the maximum extent of the broad component, and depending on the geometry of the CSM, can be considered a proxy for the velocity of the forward shock or the fastest component of the expanding SN ejecta. With respect to the intermediate-width component, Gaussian fits provide a robust measure of the average velocity of the post-shock gas. The resulting FWHM velocity of the intermediate-width component (top panel) and BVZI of the broad component (bottom panel) are plotted in Figure 15.

As revealed by Figure 15, at early times the BVZI of the broad component reaches $\sim$ 18,000 km s^{-1} and $\sim$ 16,000 km s^{-1} in SN 2005ip and SN 2006jd, respectively. Although it is difficult to accurately estimate the BVZI of SN 2006jd beyond 500 days, under close scrutiny it is observed to evolve from $\sim$ 8000 km s^{-1} to $\sim$ 7000 km s^{-1} between day 930 to 1540. As our spectroscopic coverage of SN 2005ip is limited, we turn to the measurement of Smith et al. (2009), which indicate BVZI reached $\gtrsim$ 15,000 km s^{-1} by day 400, and remained at this velocity beyond day 905 (see solid blue line in Figure 15). We note that the last several of these BVZI measurements appear to be based on extrapolation and therefore should probably be considered as an upper limit.

Turning to the time-evolution of the intermediate-width component, Figure 15 shows that over the first $\sim$ 150 days the FWHM velocity in both objects reaches maximum values of $\sim$ 1900 km s^{-1} and $\sim$ 1700 km s^{-1} in SNe 2005ip and 2006jd, respectively. Subsequently, the FWHM velocity remains relatively constant dropping down to only $\sim$ 1500 km s^{-1} over the duration of our observations.

Returning to the time-series plotted in Figure 14 (see also below, Figure 18), unlike SN 2005ip, the flux contained within the intermediate-width component of SN 2006jd is seen to dramatically increase from day 187 to 414. This period coincides with the onset of the plateau phase seen in the light curves, and is driving the excess of flux observed in the r-band light curve. In Section 4.3 the BVZI and FWHM velocity measurements are used to indicate the location of the warm and cold dust components.

4. DISCUSSION

4.1. Comparison of 1988Z-like SNe IIn

Objects within the 1988Z-class exhibit strikingly similar characteristics, however as we have already shown, subtle differences do exist between SNe. These differences can be used to decipher the nature of the CSM and provide insight on the progenitors. We now proceed to compare and contrast the main observational characteristics of SNe 2005ip and 2006jd.

Turning to their spectroscopic appearance, plotted in Figure 16 are early phase (top panel) and late phase (bottom panel) spectra of SNe 1988Z (Turatto et al. 1993), 2005ip, and 2006jd. Clearly, the overall appearance of these objects is remarkably similar at both early- and late-times. At early epochs each spectrum is dominated by a broad Hα component exhibiting similar BVZI and FWHM values, and as noted earlier, an excess of blue continuum flux which is powered by numerous Fe II emission lines (e.g., see Foley et al. 2007). At late times the FWHM velocity of the intermediate-width component and the relative strength of the Hα feature are nearly identical. Close similarities also appear between the relative strength and FWHM velocity of the He I, [O III] $\lambda\lambda$4363, 4959, 5007, the Ca II near-IR triplet, and many of the coronal emission lines.

In Figure 17 we compare the absolute B-, V- and r/R-band light curves of SNe 1988Z (Turatto et al. 1993), 2005ip and 2006jd. This comparison provides evidence of additional observational diversity amongst members of this class of SNe IIn. With the caveat in mind that the explosion epochs of these SNe are not well constrained, at early epochs SN 1988Z is found to be $\sim$ 1.5 mag brighter than SNe 2005ip and 2006jd. The photometric evolution over the first $\sim$ 200 days is nearly identical in each SN. Beyond this point SN 1988Z exhibits an inflection point followed by a slow, linear decline, while SNe 2005ip and 2006jd exhibit a phase characterized by constant emission. In the case of SN 2005ip, however, its brightness during this plateau phases is ~ -14 mag, while in SN 2006jd the absolute magnitude is, depending on the specific bandpass, between -16 to -17 mag. Interestingly, as observed in Figure 17, by day $\sim$ 1500 all three objects exhibit nearly identical magnitudes in the B- and V-band light curves of ~ -13 mag.

4.2. Insight on the progenitor of SN 2006jd

Figure 18 presents a comparison of the soft X-ray (0.2$-$10 keV) and Hα luminosities of SNe 2005ip and 2006jd. The X-ray measurement of SN 2005ip is from Immler & Pooley (2007), and those of SN 2006jd were recently reported by Chandra et al. (2012). Also included in the figure is the absolute r-band light curve of SN 2006jd. This comparison reveals that during the plateau phase when SN 2006jd clearly outshone SN 2005ip at optical/near-IR wavelengths, the X-ray (and Hα) luminosity of SN 2006jd roughly exceeds SN 2005ip by an order of a magnitude. Interestingly, the X-ray luminosity of SN 2006jd appears to remain relatively constant for at least $\sim$ 600 days.

A detailed discussion of the X-ray luminosity is presented by Chandra et al. (2012), nevertheless here we speculate that the flat evolution observed in the X-ray light curve of SN 2006jd may result from the SN blast wave interacting with a dense, torus-like shell of material located equatorially around the SN, akin to what is observed in η Carinae (Smith 2006). As the SN blast wave interacts with this shell of material radiative shocks produce copious amounts of X-rays, which in turn, gives rise to: (i) the plateau phase of the optical light curves, (ii) the significant strengthening over time of the intermediate-width component of Hα, hence the r-band excess, (iii) the various emission lines that exhibit intermediate-width components and, (iv) the coronal lines which are formed from photo-ionization of the pre-SN wind. In this model the broad Hα component is then formed from the SN blast wave interacting with the rarified progenitor wind located in the polar directions of the progenitor star, perpendicular to the plane of the dense shell (e.g. Blondin, Lundqvist & Chevalier 1996). The equatorial shell likely originates from a pre-SN LBV eruption. Such a shell can explain both the $> 10^6$ cm^3 gas density measured from the [O III] $\lambda5007/\lambda4363$ ratio, and a portion of the near-IR emission corresponding to warm dust, which we estimate in Section 3.4 to be located $\sim 2.5{\times}10^{16}$ cm from the progenitor star.

The diversity of the X-ray luminosities exhibited in Figure 18 is likely due to differences in the density and/or geometry of the CSM which is shocked by the SN blast wave. When CS interaction dominates radioactivity and the shock wave is radiative the total X-ray luminosity depends on the CS density, shock radius, R, and velocity, V, as $L \propto \rho_{CSM} R^2 V^3$. For a steady, spherically symmetric wind $L \propto \dot{M} V^3 \approx$ constant. In the case of an anisotropic or clumpy CSM the latter relation is not necessarily valid, and the luminosity depends on the exact density distribution. Most of the luminosity produced from the shock interaction is emitted as X rays. A fraction of this energy is emitted inwards towards the SN ejecta and is reprocessed into optical/UV lines (Chevalier & Fransson 1994), while part of the outgoing X-ray flux may be absorbed by the CSM, and there re-radiated as narrow optical/UV lines, or escape. There is therefore a direct relation between the CS density and both the X-ray flux and the optical/UV flux from the SN, and this applies to the high density CSM measured in SN 2006jd.

The higher levels of optical emission observed in SN 2006jd over SN 2005ip at later phases (see Figure 17) is best explained by a higher density of CS material that forms the intermediate-width velocity (post-shock gas) component. Furthermore, the ‘bump’ exhibited by the r-band light curve of SN 2006jd is more naturally explained with a shell like geometry of dense material, as is seen in LBVs like η Carinae, and less aligned with expectations from a steady- or clumpy-wind scenario.

Within this context, the lower X-ray luminosity and gas densities (Smith et al. 2009) observed in SN 2005ip, along with the appearance of high-ionization coronal lines observed at the earliest times, suggest that the mass-loss mechanism of its progenitor was less extreme. As advocated by Smith et al. (2009), it appears more likely that SN 2005ip exploded while enshrouded in a relatively spherical, clumpy-wind environment.

4.3. Location of the warm and cold dust components

Armed with the warm and cold BB radii (R_w and R_c) computed in Section 3.4, in combination with velocity estimates of the forward and reverse shocks obtained from measurements made in Section 3.5.3, we endeavor to constrain the location of both dust components in SN 2005ip and SN 2006jd. Plotted in each panel of Figure 19 is the location of R_w and R_c. Here R_c is given for a range of covering factor (see below), where values below 4π account for deviations from spherical symmetry. Also plotted in Figure 19 is the position of the forward shock determined from the BVZI value of the broad Hα component, and the location of the reverse shock as dictated by the BVZI of intermediate-width component, which has been computed by taking three sigma of the measured FWHM velocity shown in Figure 15. Finally, plotted in Figure 19 are dust evaporation radii, R_{evap}, for three grain sizes. These curves represent a cavity around the SN in which all dust is evaporated by the radiation field produced from the initial shock break-out. To estimate R_{evap} we make use of the following expression (e.g. Fox et al. 2010)

$$R_{evap} = \left(\frac{L_{max} < Q >}{16\pi\sigma T_{evap}^4} \right)^{1/2}, \tag{3}$$

which is valid under the assumption that the dust is optically thin. Here L_{max} is the maximum bolometric luminosity of the SN, $< Q >$ is the ratio of the Planck averaged dust absorption efficiency to the dust emission efficiency, σ is the Stefan-Boltzmann constant, and T_{evap} is the evaporation temperature ($\sim$ 1900 K for graphite). The parameter $< Q >$ depends upon the evaporation temperature of the dust, the grain size of the dust, and the temperature of the SN. For our calculations of R_{evap} we adopted values of $T_{evap} = 1900$ K and $T_{SN} = 7000$ K. This value of T_{SN} was determined from the BB_h fits presented in Section 3.3 (see Table 8). Our earliest observations of SNe 2005ip and 2006jd indicate $L_{max} \sim 3.2\times10^{42}$ erg s^{-1} or 8.3×10^{8} $L_{\odot}$, however it is probably somewhat higher before the discovery dates. For a peak luminosity of 10^9 $L_{\odot}$ and a graphite composition with grain radii of $a = 1.0$ μm, 0.1 μm and 0.01 μm, we obtain as shown in Figure 19, values of R_{evap} of $\sim 1.5\times10^{16}$ cm, $\sim 3.0\times10^{16}$ cm and $\sim 5.0\times10^{16}$ cm, respectively. Unfortunately, R_{evap} also depends sensitively on the grain composition, for instance in the case of a silicate dust composition, R_{evap} could be a factor of $\sim$ 5 higher (Dwek 1985). Therefore, 1.5×10^{16} cm should be considered a minimum radius for dust evaporation.

Figure 19 suggests that the warm dust component in SN 2005ip formed well within the CDS during the first several months after the SN explosion. However, as revealed from the right panel of Figure 19, the warm dust component of SN 2006jd appears to precede the forward shock and R_{evap} for grain size of $a = 0.1$ and 1 μm for the initial 200 days of evolution, whereupon the forward shock surpasses the warm dust R_w.

This finding raises some perplexing questions. First of all, how does the warm dust component in SN 2006jd find itself to be located beyond the forward shock during the first ~ 200 days, and how does this dust component survive once it is swept up by the SN blast wave? On day 9 the warm dust R_w is computed to be $\sim 2.5{\times}10^{16}$ cm, while the shock radius only reaches $\sim 1.6{\times}10^{15}$ cm. If a portion of the warm dust actually lies beyond the forward shock, this would imply that it is pre-existing and was ejected by the progenitor star prior to exploding in a shell at a minimum distance of $\sim 2.5{\times}10^{16}$ cm. However, at the earliest phases this pre-existing warm dust component could be evaporated from the initial SN outburst.

A solution of this problem could be that the CSM of the SN is highly anisotropic, e.g., a bipolar structure with a disk like dense equatorial region, as was discussed in Section 4.2. The dust would then be pre-existing in the CSM and heated by the radiation from the SN. In this case the SN would expand roughly spherically until the equatorial disk is encountered. The interaction between the ejecta and disk would then slow down the equatorial region of the ejecta, while the polar region of the ejecta would expand largely unimpeded. This would explain the larger radius of the dust emitting region compared to the blast wave at early times, and the opposite situation at late times. As was discussed in the previous sub-section, this picture is consistent with the evolution of the Hα line, which changes in both shape and intensity at an epoch corresponding to $\sim R_w/V_{max} \sim 170 \cdot (R_w/1.5 \times 10^{16}\ \mathrm{cm})(V_{max}/10^4\ \mathrm{km\ s^{-1}})^{-1}$ days, which signals the encounter of the ejecta with CS shell.

An equatorial shell may also explain the evolution of the Hα line shape. At 22 days the line extends to $\sim 16,000$ km s^{-1} on the blue side and ~ 8000 km s^{-1} on the red (see right panel of Figure 14). This asymmetry may be a result of occultation of the receding side of the ejecta by the opaque photosphere. If the photosphere has a radius, R_p, and the maximum radius of the ejecta is, $R_{max}(= V_{max}t)$, the extent on the red side in the case of homologous expansion will be $V_{red} = V_{max}(1 - (R_p/R_{max})^2)^{1/2}$. For the above values we get $R_p/R_{max} \sim 0.87$ at 22 days.

As long as the radius of the ejecta is smaller that the inner radius of the shell, the Hα emission from the receding ejecta will be seen as a red wing. However, once the radius of the ejecta becomes larger than the shell, the red wing of the Hα line will only be seen if the optical depth of the dust in the shell is low. If this is not the case the extent of the red wing will rapidly decrease, while the blue wing will remain largely unaffected. This is consistent with what is seen from 41 days to 124 days as illustrated in the right panel of Figure 10. If any of the pre-existing dust survives the initial radiation field associated with the SN outburst, then the increased asymmetry observed in the Hα line profile could be caused by obscuration due to dust absorption. This scenario does not exclude the possibility that dust condensation occurs within the CDS at late epochs, but does not require it either. It does, however, solve the problem with the location of the warm dust relative to the SN blast wave. At the same time it also explains the early indication of dust emission seen, which is a problematic to explain solely by newly formed dust.

The intermediate Hα component is seen to increase in both luminosity and width during the first few hundred days (see Figure 14). As mentioned previously, the dramatic increased prominence of the intermediate component is driven by the SN shock wave moving into the dense CS shell, with a velocity of $V_{disk} \sim V_{ej}(\rho_{ej}/\rho_{disk})^{1/2} \ll V_{ej}$. A reverse shock into the ejecta would then have a velocity of $V_{ej} - V_{disk} \approx V_{ej}$ in the observer frame. At the time of this interaction we expect to observe an increase in both the luminosity of the intermediate component from the shock going into the disk and of the ejecta component from the reverse shock into the ejecta, and possibly also X ray-ionized ejecta in the plane of the shell.

Alternatively, the last non-detection date of SN 2006jd in KAIT search images occurred $\sim$ 170 days before discovery, implying that there is a possibility that the explosion epoch could be significantly earlier than the discovery date. If the SN did occur some $\sim$ 5 months prior to discovery then the forward shock radius at $\sim$ 200 days would be comparable to R_w. This would then suggest that the warm dust formed in the vicinity of the forward shock. However, if the progenitor exploded significantly prior to discovery, this would imply that SN 2006jd was substantially brighter than SNe 1988Z and 2005ip. Given the nature of the SED at the time of our first observations, we, however, believe the explosion of SN 2006jd did not occur long before the time of discovery.

Turning to the location of the cold, pre-existing dust component, as demonstrated in Figure 19, R_c varies significantly as a function of the adopting covering factor (CF). For spherical symmetry CF $= 4\pi$, however, in the case of SNe IIn it is not obvious that such a case is appropriate. In fact, observations suggest that the majority of LBVs are surrounded by shells of dense material, and also exhibit enhanced brightness regions that are aligned to a preferred axis of symmetry (Nota et al. 1995). For example, the well-studied LBV-candidate HD 167625 displays strong evidence for a pre-existing cold ($T_{BB} \sim 130$ K) dust component which is distributed within an equatorially enhanced torus inclined 60^o with respect to the observer (Hutsemekérs et al. 1994; O'hara et al. 2003). The measured geometry of this shell implies a CF $= 2\pi$. Given the indications described earlier that the CSM surround

SN 2006jd resides in a dense equatorial torus, an appropriate CF would place the cold dust well beyond the location implied by spherical symmetry, and as indicated in Figure 19, also just beyond the fast forward shock plowing through CSM in the polar direction. In the case of SN 2005ip where the CS environment appears to be more consistent with a clumpy wind, the cold dust component is also likely described by a CF that deviates significantly from spherical symmetry (see Fox et al. 2010). We again stress that a spherically symmetric CF provides lower limits on R_w and R_c, and our ability to constrain these parameters is dependent on a large number of underlying assumptions.

5. CONCLUSIONS

The observational properties of SN 2006jd and SN 2005ip have a number of similarities with the 1988Z-like subclass of SN IIn. However differences are also evident, most notably between their light curve morphologies, X-ray luminosities, and the ionization potentials of the coronal lines and the time-scale in which these features appear. These differences are most likely traced back to the mass-loss history of the progenitors. With densities on the order of $> 10^6$ cm^{-3}, and an X-ray luminosity an order of a magnitude higher than in SN 2005ip, the progenitor of SN 2006jd likely experienced a significant mass-loss event during its late-state evolution akin to the great 19th century eruption of η Carinae. In the case of SN 2005ip, its CSM was comparably less dense and probably clumpy (Smith et al. 2009), explaining both the lower X-ray luminosity and the early turn-on of high-ionization coronal lines. Within this context one could then expect a continuum of SN IIn luminosities to trace the mass-loss history, with the most luminous objects like SN 2006gy exploding in the midst of, or soon after, an LBV-like outburst (e.g. Moriya et al. 2012); while the more moderately luminous objects, like SN 2006jd, find themselves exploding in the centuries or eons after suffering an eruptive LBV outburst. Given the differences between SN 2006jd and SN 2005ip, it appears that the mass-loss mechanism of the latter may be more aligned with a super-wind or perhaps mass-ejections of a less extreme nature.

We calculate that both SN 2005ip and SN 2006jd are associated with similar amounts of warm ($\sim 10^{-4}$ M$_\odot$) and cold ($\sim 10^{-2}$ M$_\odot$) dust. Given the uncertainties involved in the derivations, it is encouraging to note that these estimates are consistent with the dust masses computed for other SNe IIn (e.g. Gerardy et al. 2002; Pozzo et al. 2004; Meikle et al. 2007; Andrews et al. 2011; Gall, Hjorth, & Andersen 2011).

This material is based upon work supported by NSF under grants AST–0306969, AST–0908886, AST–0607438, and AST–1008343. The Oskar Klein Centre is funded by the Swedish

Research Council. C. F. acknowledges support from the Swedish Research Council and the Swedish National Space Board. O.D. Fox would like to thank the NASA Postdoctoral Program fellowship for support. J. P. Anderson and M. Hamuy acknowledge support by CONICYT through FONDECYT grant 3110142, and the Millennium Center for Supernova Science (P10-064-F). The Dark Cosmology Centre is funded by the Danish National Research Foundation. The Isaac Newton Telescope is operated on the island of La Palma by the Isaac Newton Group in the Spanish Observatorio del Roque de los Muchachos of the Instituto de Astrofísica de Canarias. Also based on observations made with the Nordic Optical Telescope, operated on the island of La Palma jointly by Denmark, Finland, Iceland, Norway, and Sweden, in the Spanish Observatorio del Roque de los Muchachos of the Instituto de Astrofisica de Canarias.

REFERENCES

Agnoletto, I., Benetti, S., Cappellaro, E., et al. 2009, ApJ, 691, 1348

Andrews, J. E., Clayton, G. C., Wesson, R., et al. 2011, AJ, 142, 45

Asplund, M., Grevesse, N., Sauval, A. J., & Scoot, P. 2009, ARA&A, 47, 481

Benetti, S., Cappellaro, E., Turatto, M., et al. 2006, ApJ, 653, L129

Blondin, J. M., Lundqvist, P., & Chevalier, R. 1996, ApJ, 472, 257

Blondin, S., Modjaz, M., Kirshner, R., et al. 2006, CBET , 679, 1

Boles,T., Nakano, S., & Itagaki, K. 2005, IAU Circ., 275, 1

Branch, D., Falk, S. W., Uomoto, A. K., et al. 1981, ApJ, 244, 780

Breeveld, A. A., Landsman, W., Holland, S. T., et al. 2011, in AIP Conf. Proc. 1358, Gamma-Ray Bursts 2010, ed. J. E. McEnergy, J. L. Racusin, & N. Gehrels (Melville, NY: AIP), 373; arXiv:1102.4717

Brown, P. J., Holland, S. T., Immler, S., et al. 2009, AJ, 137, 4517

Cardelli J. A., Clayton G. C., & Mathis J. S. 1989, ApJ, 345, 245

Chandra, P., & Soderberg, A. 2007, ATel, 1290, 1

Chandra, P., et al. 2012, submitted to ApJ

Chatzopoulos, E., Wheeler, J. C., Vinko, J., et al. 2011, ApJ, 729, 143

Chevalier, R. A., & Fransson, C. 1994, ApJ, 420, 268

Chevalier, R. A., & Irwin, C. M., 2011, ApJ, 729, L6

Chevalier, R. A., & Irwin, C. M., 2012, ApJ, 747, L17

Chugai, N. N., & Danziger, I. J. 1994, MNRAS, 268, 173

Chugai, N. N., Blinnikov, S., Cumming, R. J., et al. 2004, MNRAS, 352, 1213

Contreras, C., Hamuy, M., Phillips, M. M., et al. 2010, AJ, 139, 519

Deng, J., Kawabata, K. S., Ohyama, Y., et al. 2004, ApJ, 605, L37

Dessart, L., Hillier, J. D., Suvi, G., et al. 2009, MNRAS, 394, 21

Dopita, M. A., Cohen, M., Schwartz, R. D., & Evans, R. 1984, ApJ, 287, 69

Dwek, E. 1985, ApJ, 297, 719

Foley, R. J., Smith, N., Ganeshalingam, M., et al. 2007, ApJ, 657, 105

Fox, O. D., Skrutskie, M. F., Chevalier, R. A., et al. 2009, ApJ, 691, 650

Fox, O. D., Chevalier, R. A., Dwek, E., et al. 2010, ApJ, 725, 1768

Fox, O. D., Chevalier, R. A., Skrutskie, M. F., et al. 2011, ApJ, 741, 7

Fransson, C., Chevalier, R. A., Filippenko, A. V., et al. 2002, ApJ, 572, 350

Gall, C., Hjorth, J., & Andersen, A. C. 2011, A&A Rev., 19, 43

Gerardy, C. L., Fesen, R. A., Nomoto, K., et al. 2002, ApJ, 575, 1007

Germany, L. M., Reiss, D. J., Sadler, E. M., Schmidt, B. P., & Stubbs, C. W. 2000, ApJ, 533, 320

Gröningsson, P., Fransson, C., Lundqvist, P., et al. 2006, A&A, 456, 581

Hamuy, M., Phillips, M. M., Suntzeff, N. B., et al. 2003, Nature, 424, 651

Hamuy, M., Folatelli, G., Morrell, N. I., et al. 2006, PASP, 118, 2

Heger, A., Jeannin, L., Langer, N., & Baraffe, I. 1997, A&A, 327, 224

Henry, R. B. C., & Branch, D. 1987, PASP, 99, 112

Hoffman, J. L., Leonard, D. C., Chornock, R., et al. 2008, ApJ, 688, 1186

Hutsemekers, D., van Drom, E., Gosset, E., & Melnick, J. 1994, A&A, 290, 906

Immler, S., & Pooley, D. 2007, ATel, 1004, 1

Immler, S., Brown, P. J., Filippenko, A. V., & Pooley, D. 2007, ATel, 1290, 1

Kankare, E., et al. 2012, MNRAS, submitted

Kewley, L. J., & Dopita, M. A. 2002, ApJS, 142, 35

Kiewe, M., Gal-Yam, A., Arcavi, I., et al. 2012, ApJ, 744, 10

Landolt, A. U. 1992, AJ, 104, 340

Meikle, W. P. S., Mattila, S., Pastorello, A., et al. 2007, ApJ, 665, 608

Miller, A. A., Silverman, J. M., Butler, N. R., et al. 2010, MNRAS, 404, 305

Moriya, T. J., Blinnikov, S. I., Tominaga, N., et al. 2012, submitted, arXiv:1204.6109

Nota, A., Livio, M., Clampin, M., & Schulte-Ladbeck, R. 1995, ApJ, 448, 788

O'Hara, T. B., Meixner, M., Speck, A. K., Ueta, T., & Bobrowsky, M. 2003, ApJ, 598, 1255

Ofek, E. O., Cameron, P. B., Kasliwal, M. M., et al. 2007, ApJ, 659, L13

Pastorello, A., Turatto, M., Benetti, S., et al. 2002, MNRAS, 333, 27

Pastorello, A., Valenti, S., Zampieri, L., et al. 2009, MNRAS, 394, 2266

Persson, S. E., Murphy, D. C., Krzeminski, W., Roth, M., & Rieke, M. J. 1998, AJ, 116, 2475

Pettini, M., & Pagel, B. E. J. 2004, MNRAS, 348, 59

Pozzo, M., Meikle, W. P. S., Fassia, A., et al. 2004, MNRAS, 352, 457

Prasad, R. R., & Li, W. 2006, CBET, 673, 1

Quimby, R. M., Aldering, G., Wheeler, J. C., et al. 2007, ApJ, 668, L99s

Roming, P. W. A., Kennedy, T. E., Mason, K. O., et al. 2005, Space Sci. Rev., 120, 95

Schlegel, E. M. 1990, MNRAS, 244, 269

Schlegel, D. J., Finkbeiner, D. P., & Davis, M. 1998, ApJ, 500, 525

Smith, J. A., Tucker, D. L., Kent, S., et al. 2002, AJ, 123, 2121

Smith, N. 2006, ApJ, 644, 1151

Smith, N., & McCray, R. 2007, ApJ, 671, L17

Smith, N., Li, W., Foley, R. J., et al. 2007, ApJ, 666, 1116

Smith, N., Chornock, R., Li, W., et al. 2008, ApJ, 686, 467

Smith, N., Silverman, J. M., Chornock, R., et al. 2009, ApJ, 695, 1334

Smith, N., Hinkle, K. H., & Ryde, N. 2009b, ApJ, 137, 3558

Smith, N., Silverman, J. M., Filippenko, A. V., et al. 2012, AJ, 143, 17

Sollerman, J., Cumming, R. J., & Lundqvist, P. 1998, ApJ, 493, 933

Turatto, M., Cappellaro, E., Danziger, I. J., et al. 1993, MNRAS, 262, 128

Turatto, M., Suzuki, T., Mazzali, P. A., et al. 2000, ApJ, 534, L57

Turner, K., & Pearce, G. 1992, Ap&SS, 190, 1

Woosley, S. E., Blinnikov, S., & Heger, A. 2007, Nature, 450, 390

Yoon, S.-C., & Cantiello, M. 2007, ApJ, 717, L62

This preprint was prepared with the AAS LaTeX macros v5.2.

Table 1. Local Sequences of SNe 2005ip and 2006jd in the Standard System

STAR ID	R.A.	Decl.	u'	g'	r'	i'	B	V	Y	J	H	K_s
						SN 2005ip						
01	09:32:15.63	+08:24:43.82	···	···	···	···	···	···	11.890(008)	11.684(007)	11.428(007)	···
02	09:32:13.24	+08:27:15.47	15.560(033)	···	···	···	14.658(007)	14.048(014)	13.183(008)	12.956(006)	12.654(006)	···
03	09:32:20.99	+08:26:13.89	17.726(018)	15.625(010)	14.843(007)	14.531(006)	16.134(012)	15.176(009)	13.716(009)	13.368(008)	12.874(007)	···
04	09:32:14.03	+08:26:12.68	17.276(015)	15.550(010)	14.921(007)	14.708(006)	15.999(008)	15.179(009)	13.996(007)	13.699(006)	13.282(007)	···
05	09:32:16.12	+08:30:07.69	18.475(036)	15.955(011)	15.019(007)	14.695(007)	16.519(011)	15.434(006)	13.876(010)	13.519(009)	13.003(007)	···
06	09:32:15.71	+08:24:18.79	17.918(014)	16.076(008)	15.416(006)	15.191(006)	16.538(007)	15.693(008)	14.457(008)	14.145(007)	13.706(007)	···
07	09:32:24.28	+08:30:15.54	18.271(034)	16.445(009)	15.742(007)	15.460(007)	16.913(014)	16.044(007)	14.704(014)	14.388(012)	13.887(011)	···
08	09:32:16.41	+08:24:38.99	17.864(025)	16.663(012)	16.234(008)	16.092(006)	17.002(007)	16.396(007)	15.489(009)	15.242(008)	14.926(012)	···
09	09:32:20.49	+08:26:11.93	19.223(038)	17.095(011)	16.326(006)	16.055(006)	17.630(008)	16.652(009)	···	···	···	···
10	09:32:16.60	+08:29:19.12	18.394(029)	16.964(010)	16.462(006)	16.294(006)	17.344(007)	16.650(006)	15.664(011)	15.390(010)	15.059(016)	···
11	09:31:57.50	+08:26:07.65	19.668(101)	17.409(016)	16.462(006)	16.096(006)	17.952(009)	16.890(006)	···	···	···	···
12	09:31:54.46	+08:28:01.39	17.907(024)	16.917(009)	16.593(008)	16.465(008)	17.204(007)	16.715(006)	···	···	···	···
13	09:31:57.32	+08:26:57.25	18.633(024)	17.190(011)	16.642(008)	16.426(006)	17.601(008)	16.858(008)	···	···	···	···
14	09:32:23.92	+08:30:04.83	19.141(047)	17.428(009)	16.807(007)	16.605(007)	17.872(012)	17.063(016)	···	···	···	···
15	09:32:17.64	+08:25:39.73	18.914(029)	17.645(011)	17.159(010)	16.989(007)	18.004(009)	17.338(007)	16.352(013)	16.075(013)	15.705(018)	···
16	09:32:14.88	+08:26:35.63	···	18.832(019)	17.453(012)	16.601(010)	19.546(030)	18.054(016)	15.396(010)	14.955(006)	14.331(007)	···
17	09:32:20.10	+08:25:58.43	···	18.714(015)	17.767(008)	17.394(007)	19.276(024)	18.175(009)	16.518(010)	16.150(013)	15.569(013)	···
18	09:32:03.16	+08:25:19.58	20.256(208)	18.493(008)	17.803(007)	17.555(007)	18.936(025)	18.080(008)	16.801(014)	16.469(014)	16.017(026)	···
19	09:32:07.43	+08:30:15.63	···	19.397(018)	18.018(010)	16.644(011)	20.265(055)	18.596(014)	15.132(012)	14.629(008)	14.044(009)	···
20	09:32:12.68	+08:29:08.69	···	19.550(020)	18.313(008)	17.788(008)	20.170(062)	18.889(018)	16.808(019)	16.375(022)	15.692(017)	···
21	09:32:17.38	+08:24:07.50	···	18.873(015)	18.437(012)	18.297(014)	19.147(032)	18.606(012)	···	···	···	···
22	09:31:59.77	+08:24:46.23	20.242(099)	18.989(011)	18.402(014)	18.001(011)	19.381(025)	18.599(016)	···	···	···	···
23	09:31:57.95	+08:28:48.65	20.104(157)	19.326(019)	18.848(018)	18.668(035)	19.670(033)	19.049(018)	···	···	···	···
24	09:31:57.94	+08:29:35.05	···	20.545(055)	19.156(021)	18.329(012)	21.531(186)	19.796(039)	···	···	···	···
25	09:32:10.29	+08:28:28.85	···	20.651(060)	19.333(021)	18.588(024)	21.290(246)	19.983(043)	···	···	···	···
26	09:32:17.25	+08:22:57.90	···	···	···	···	···	···	12.277(012)	11.966(010)	11.536(009)	···
27	09:32:19.74	+08:22:25.79	···	···	···	···	···	···	14.229(014)	13.923(011)	13.500(010)	···
28	09:32:23.51	+08:22:31.37	···	···	···	···	···	···	15.265(012)	14.833(015)	14.221(011)	···
29	09:32:07.26	+08:22:24.42	···	···	···	···	···	···	15.405(010)	14.960(010)	14.461(013)	···
30	09:32:26.86	+08:27:18.68	···	···	···	···	···	···	15.486(010)	15.085(009)	14.448(009)	···
31	09:32:20.35	+08:21:14.18	···	···	···	···	···	···	15.492(012)	15.213(013)	14.860(014)	···
32	09:32:29.01	+08:22:24.85	···	···	···	···	···	···	15.809(011)	15.465(014)	15.075(011)	···
33	09:32:18.96	+08:26:16.51	···	···	···	···	···	···	16.385(010)	15.809(010)	15.322(009)	···
34	09:32:32.65	+08:20:48.73	···	···	···	···	···	···	16.370(016)	16.077(014)	15.765(025)	···
35	09:32:32.86	+08:25:49.37	···	···	···	···	···	···	16.632(014)	16.097(013)	15.593(012)	···
36	09:32:21.46	+08:26:46.25	···	···	···	···	···	···	17.111(020)	16.589(017)	15.988(017)	···
37	09:32:03.40	+08:24:08.96	···	···	···	···	···	···	17.503(025)	16.996(021)	16.415(028)	···
38	09:32:16.02	+08:22:14.84	···	···	···	···	···	···	17.485(027)	17.254(039)	16.867(056)	···
39	09:32:04.01	+08:26:45.42	···	···	···	···	···	···	17.781(035)	17.359(037)	16.956(055)	···
40	09:32:31.39	+08:30:59.44	···	···	···	···	···	···	16.086(020)	15.729(009)	15.162(024)	···
41	09:32:11.66	+08:24:34.09	···	···	···	···	···	···	16.369(009)	15.850(010)	15.168(009)	···
42	09:32:05.43	+08:21:30.85	···	···	···	···	···	···	16.601(014)	16.084(018)	15.394(021)	···
						SN 2006jd						
01	08:02:19.48	+00:48:13.64	···	···	···	···	···	···	12.037(004)	11.842(006)	11.595(005)	···
02	08:02:16.88	+00:46:15.74	15.796(016)	···	···	···	···	···	···	···	···	···
03	08:02:14.35	+00:47:14.17	16.288(009)	···	···	···	15.227(008)	···	···	···	···	···
04	08:02:04.82	+00:46:44.54	15.806(016)	···	···	···	14.802(011)	···	···	···	···	···
05	08:02:04.61	+00:50:32.68	···	···	···	···	···	···	11.513(006)	11.147(010)	10.656(010)	···
06	08:02:04.17	+00:45:01.01	18.042(017)	15.829(014)	14.980(013)	14.694(011)	16.345(005)	15.340(010)	···	···	···	···
07	08:01:54.05	+00:46:03.90	16.605(009)	15.524(015)	15.199(011)	15.095(012)	15.798(005)	15.309(006)	···	···	···	···

Table 1—Continued

STAR ID	R.A.	Decl.	u'	g'	r'	i'	B	V	Y	J	H	K_s
08	08:02:20.33	+00:45:01.33	17.113(010)	15.853(012)	15.382(006)	15.245(012)	16.218(005)	15.558(005)	...	...	...	...
09	08:01:56.97	+00:47:22.42	17.067(010)	15.824(011)	15.404(008)	15.272(007)	16.172(005)	15.559(005)	...	...	...	...
10	08:01:57.06	+00:49:16.39	17.567(017)	15.952(009)	15.372(008)	15.176(008)	16.384(006)	15.596(006)	...	...	...	...
11	08:02:16.35	+00:51:28.98	17.038(013)	15.849(009)	15.429(007)	15.279(007)	16.197(005)	15.581(005)	...	...	...	...
12	08:02:13.17	+00:47:46.72	18.961(037)	16.495(011)	15.489(009)	15.134(008)	17.078(005)	15.940(006)	14.275(005)	13.903(006)	13.365(004)	...
13	08:02:14.43	+00:48:21.49	17.764(014)	16.146(010)	15.516(006)	15.278(011)	16.594(005)	15.764(005)	...	...	...	...
14	08:02:00.31	+00:47:41.50	17.071(011)	15.900(009)	15.520(006)	15.402(006)	16.222(005)	15.656(005)	...	...	...	...
15	08:02:08.48	+00:50:00.31	17.098(015)	16.003(008)	15.678(006)	15.584(008)	16.301(005)	15.794(004)	...	...	...	...
16	08:01:59.72	+00:44:21.48	18.363(087)	16.440(013)	15.721(007)	15.461(007)	16.942(007)	16.000(006)	...	...	...	...
17	08:01:52.81	+00:51:27.65	17.090(010)	16.019(006)	15.739(005)	15.648(005)	16.288(005)	15.829(005)	...	...	...	...
18	08:02:19.20	+00:50:48.30	17.744(017)	16.334(006)	15.834(005)	15.666(005)	16.731(005)	16.027(004)	...	...	...	...
19	08:01:55.16	+00:44:40.06	17.514(023)	16.346(006)	15.934(005)	15.794(005)	16.678(005)	16.087(005)	...	...	...	...
20	08:02:12.15	+00:48:40.00	17.767(015)	16.406(008)	15.875(005)	15.675(006)	16.809(005)	16.079(004)	14.979(004)	14.714(007)	14.350(005)	...
21	08:02:10.86	+00:49:11.78	18.235(039)	16.872(006)	16.303(005)	16.074(005)	17.280(005)	16.531(004)	15.369(005)	15.083(007)	14.687(005)	...
22	08:01:53.31	+00:47:23.35	18.221(150)	16.916(008)	16.360(005)	16.156(005)	17.316(005)	16.576(004)	...	...	...	...
23	08:02:02.96	+00:46:22.33	17.935(029)	16.808(008)	16.411(005)	16.268(005)	17.121(005)	16.556(004)	...	...	...	...
24	08:02:12.92	+00:46:00.44	18.478(025)	17.313(006)	16.852(005)	16.689(005)	17.678(006)	17.030(004)	...	...	...	...
25	08:01:59.37	+00:48:54.47	18.519(045)	17.398(006)	16.934(005)	16.754(006)	17.747(006)	17.114(005)	...	...	...	...
26	08:01:58.49	+00:48:21.20	19.670(070)	17.903(007)	17.173(006)	16.897(005)	18.395(006)	17.493(005)	...	...	...	...
27	08:02:29.36	+00:45:35.32	...	...	...	...	...	...	13.363(006)	13.079(009)	12.736(009)	...
28	08:02:26.29	+00:46:11.42	...	...	...	...	...	...	14.052(004)	13.721(006)	13.248(005)	...
29	08:02:24.21	+00:49:14.59	...	...	...	...	...	...	14.313(005)	14.111(006)	13.845(006)	...
30	08:02:28.22	+00:48:16.92	...	...	...	...	...	...	14.683(005)	14.304(007)	13.753(006)	...
31	08:02:16.12	+00:46:29.78	...	...	...	...	...	...	15.224(006)	14.880(006)	14.396(006)	...
32	08:02:02.04	+00:48:41.18	...	...	...	...	...	...	15.811(006)	15.414(007)	14.801(005)	...
33	08:02:01.87	+00:48:09.72	...	...	...	...	...	...	16.285(007)	16.018(008)	15.649(010)	...
34	08:02:22.32	+00:48:52.06	...	...	...	...	...	...	16.339(007)	16.009(008)	15.507(007)	...
35	08:02:04.97	+00:47:21.19	...	...	...	...	...	...	16.976(007)	16.654(011)	16.254(016)	...
36	08:02:07.43	+00:45:39.02	...	...	...	...	...	...	17.032(011)	16.598(010)	16.029(014)	...
37	08:02:14.59	+00:49:38.28	...	...	...	...	...	...	17.147(012)	16.701(019)	16.094(011)	...
38	08:02:17.31	+00:49:58.44	...	...	...	...	...	...	17.278(011)	17.052(017)	16.769(020)	...
39	08:02:16.27	+00:48:33.66	...	...	...	...	...	...	17.236(013)	16.871(013)	16.330(013)	...
40	08:02:02.16	+00:46:44.98	...	...	...	...	...	...	17.207(012)	17.026(014)	16.759(025)	...
41	08:02:14.48	+00:45:47.88	...	...	...	...	...	...	17.567(021)	17.113(017)	16.590(020)	...
42	08:02:17.91	+00:45:51.66	...	...	...	...	...	...	17.752(014)	17.334(016)	16.841(026)	...
43	08:02:05.77	+00:48:48.10	...	...	...	...	...	...	15.547(007)	15.208(006)	14.745(004)	14.557(020)
44	08:02:08.05	+00:48:06.34	...	...	...	...	...	...	15.394(006)	14.990(006)	14.368(006)	14.158(020)
45	08:02:04.41	+00:47:42.32	...	...	...	...	...	...	15.853(006)	15.668(008)	15.434(007)	...
46	08:02:05.73	+00:48:03.60	...	...	...	...	...	...	18.069(015)	17.626(014)	16.960(026)	16.571(046)
47	08:02:10.65	+00:48:47.23	...	...	...	...	...	...	15.214(006)	14.976(006)	14.673(005)	14.558(020)
48	08:02:22.43	+00:47:06.40	...	...	...	...	...	...	11.684(006)	11.318(008)	10.810(007)	...
49	08:02:22.20	+00:46:29.10	...	...	...	...	...	...	14.052(005)	13.829(006)	13.548(004)	...
50	08:02:22.15	+00:45:49.64	...	...	...	...	...	...	15.058(004)	14.644(007)	14.045(005)	...
51	08:02:26.44	+00:47:09.20	...	...	...	...	...	...	16.684(009)	16.433(009)	16.065(013)	...

Note. — One sigma uncertainties given in parentheses in thousandths of a magnitude correspond to an rms of the magnitudes obtained on photometric nights.

Table 2. Optical Photometry of SN 2005ip in the Natural System

JD–2450000+	u	g	r	i	B	V	Telescope[a]
3683.86	15.925(016)	15.375(012)	15.044(018)	15.034(018)	15.613(011)	15.215(013)	SWO
3684.86	16.029(017)	15.441(009)	15.087(011)	15.051(012)	15.700(007)	15.262(010)	SWO
3687.86	16.240(018)	15.603(009)	15.172(010)	15.130(010)	15.864(009)	15.378(010)	SWO
3689.86	16.403(014)	15.731(010)	15.218(015)	15.151(017)	16.000(009)	15.503(009)	SWO
3690.86	16.427(018)	15.815(007)	15.288(009)	15.228(011)	16.076(007)	15.564(007)	SWO
3694.86	16.655(014)	16.039(009)	15.426(015)	15.407(014)	16.295(009)	15.766(009)	SWO
3699.82	16.885(012)	16.207(012)	15.623(013)	15.611(015)	16.487(010)	15.981(011)	SWO
3702.81	16.940(012)	16.286(013)	15.693(020)	15.699(019)	16.564(010)	16.064(016)	SWO
3706.81	16.933(011)	16.252(033)	15.599(044)	15.630(049)	16.559(019)	16.074(034)	SWO
3713.84	17.026(011)	16.424(017)	15.873(019)	15.932(026)	16.703(011)	16.290(016)	SWO
3716.83	17.104(011)	16.489(020)	15.910(024)	16.015(027)	16.729(014)	16.352(018)	SWO
3721.78	17.143(019)	16.617(010)	16.024(017)	16.133(023)	16.822(012)	16.451(012)	SWO
3726.83	17.155(014)	16.593(014)	16.054(023)	16.179(028)	16.843(010)	16.459(018)	SWO
3728.83	17.198(013)	16.604(016)	16.069(021)	16.210(032)	16.855(011)	16.487(019)	SWO
3737.79	17.343(012)	16.585(054)	15.973(069)	16.174(077)	16.911(029)	16.516(047)	SWO
3739.81	17.368(017)	16.650(035)	16.044(050)	16.233(060)	16.949(023)	16.545(041)	SWO
3741.77	17.447(017)	16.762(015)	16.236(017)	16.419(023)	16.988(011)	16.625(014)	SWO
3746.78	17.564(014)	16.908(013)	16.345(020)	16.545(031)	17.145(011)	16.765(017)	SWO
3751.77	17.645(030)	17.017(015)	16.528(010)	16.718(018)	17.297(019)	16.956(018)	SWO
3755.76	17.769(033)	17.113(016)	16.521(025)	16.747(045)	17.338(021)	17.007(024)	SWO
3761.72	17.899(018)	17.180(025)	16.589(027)	16.864(035)	17.433(012)	17.084(026)	SWO
3762.71	17.938(018)	17.219(030)	16.611(034)	16.932(034)	17.483(013)	17.101(023)	SWO
3763.70	17.963(022)	17.226(022)	16.605(028)	16.912(035)	17.513(016)	17.140(023)	SWO
3764.72	17.992(019)	17.259(025)	16.646(031)	16.937(040)	17.519(019)	17.166(027)	SWO
3765.70	18.014(020)	17.280(029)	16.674(033)	16.972(040)	17.568(020)	17.209(027)	SWO
3768.72	18.053(018)	17.235(048)	16.611(056)	16.851(068)	17.559(031)	17.158(047)	SWO
3771.69	18.076(020)	17.288(047)	16.633(051)	16.920(071)	17.581(031)	17.209(047)	SWO
3772.69	18.170(021)	17.423(028)	16.798(037)	17.124(042)	17.675(019)	17.325(028)	SWO
3774.69	18.191(028)	17.480(019)	16.835(028)	17.143(037)	17.760(016)	17.425(023)	SWO
3778.68	18.284(049)	17.588(020)	17.008(016)	17.283(031)	17.892(027)	17.579(022)	SWO
3783.61	18.427(034)	17.701(016)	17.031(024)	17.352(040)	17.934(020)	17.599(024)	SWO
3786.69	18.419(023)	17.682(030)	16.984(040)	17.379(049)	17.959(019)	17.578(034)	SWO
3788.67	18.428(022)	17.670(036)	17.001(041)	17.401(048)	17.971(019)	17.607(039)	SWO
3790.66	18.542(027)	17.664(033)	17.050(040)	17.428(051)	18.023(022)	17.644(036)	SWO
3795.67	18.493(026)	17.637(055)	16.956(061)	17.333(088)	17.929(040)	17.555(060)	SWO
3799.63	18.451(035)	17.524(052)	16.849(053)	17.178(077)	17.871(041)	17.447(056)	SWO
3801.62	18.650(026)	17.890(035)	17.183(040)	17.622(053)	18.151(024)	17.804(039)	SWO
3809.62	18.741(083)	18.176(033)	17.383(019)	17.805(043)	18.441(045)	18.017(035)	SWO
3815.62	···	18.098(042)	17.308(049)	17.825(069)	18.415(024)	18.066(042)	SWO
3819.59	18.906(024)	18.071(053)	17.294(062)	17.829(074)	18.370(035)	18.095(046)	SWO
3823.59	18.920(031)	18.181(048)	17.405(047)	17.901(070)	18.492(032)	18.124(049)	SWO
3831.57	19.099(040)	18.330(036)	17.465(045)	18.054(070)	18.617(031)	18.248(041)	SWO
3838.58	19.137(094)	18.548(029)	17.540(033)	18.135(060)	18.717(051)	18.343(043)	SWO
3840.53	19.139(061)	18.477(034)	17.549(037)	18.108(064)	18.793(034)	18.437(039)	SWO
3846.56	19.125(030)	18.289(054)	17.515(042)	18.009(075)	18.625(042)	18.247(047)	SWO
3858.49	19.186(041)	18.392(084)	17.415(084)	18.004(118)	18.686(055)	18.291(081)	SWO

Table 2—Continued

JD–2450000+	u	g	r	i	B	V	Telescope[a]
3867.53	19.355(101)	18.670(039)	17.589(037)	18.217(070)	19.066(059)	18.601(043)	SWO
3872.47	19.356(036)	18.600(066)	17.545(064)	18.251(081)	18.900(043)	18.529(065)	SWO
3890.50	19.208(065)	18.435(069)	17.347(060)	17.960(111)	18.788(057)	18.333(080)	SWO
4531.66	19.412(400)	18.829(400)	17.091(400)	18.635(400)	19.306(400)	18.705(400)	DUP
5202.75	20.211(400)	19.636(400)	18.011(400)	19.057(400)	19.942(400)	19.475(400)	DUP
5244.67	20.222(400)	19.373(400)	17.543(400)	19.002(400)	19.828(400)	19.375(400)	DUP

[a] DUP and SWO correspond to the du Pont and Swope telescopes, respectively.

Note. — One sigma uncertainties given in parentheses are in millimag.

Table 3. Near-infrared Photometry of SN 2005ip

JD–2450000+	Y	J	H	Telescope[a]
3685.85	14.579(028)	14.407(023)	14.179(021)	SWO
3692.87	14.657(033)	14.546(028)	14.236(028)	SWO
3700.86	14.926(025)	14.820(026)	14.491(028)	SWO
3704.84	15.007(044)	14.951(041)	14.585(041)	SWO
3709.80	15.102(029)	15.105(031)	14.701(031)	SWO
3714.82	15.128(040)	15.152(037)	14.761(038)	SWO
3717.84	15.207(035)	15.216(040)	14.765(038)	SWO
3731.86	15.314(047)	15.371(048)	14.826(041)	SWO
3756.77	15.601(013)	15.653(015)	14.816(013)	SWO
3773.77	15.790(018)	15.705(016)	14.690(010)	DUP
3782.72	15.858(059)	15.511(053)	14.602(032)	SWO
3786.68	15.930(022)	15.744(021)	14.582(017)	DUP
3796.70	16.012(063)	15.631(057)	···	SWO
3803.62	16.077(056)	15.660(057)	14.664(041)	SWO
3810.68	16.187(067)	15.787(062)	14.731(034)	SWO
3814.66	16.222(064)	15.782(061)	···	SWO
3817.63	16.211(060)	15.787(060)	14.748(034)	SWO
3826.57	···	···	14.784(036)	SWO
3833.60	16.361(022)	16.101(023)	14.791(016)	DUP
3839.56	16.325(061)	15.808(069)	14.720(039)	SWO
3845.56	16.405(025)	16.135(023)	14.777(018)	SWO
3848.55	16.137(064)	···	14.628(040)	SWO
3860.52	16.288(058)	15.780(066)	14.676(037)	SWO
3868.52	16.326(077)	15.823(067)	14.724(035)	SWO
4466.78	16.562(028)	17.059(047)	15.657(024)	DUP
5199.77	17.694(400)	···	···	DUP
5261.57	17.224(400)	17.831(400)	16.453(400)	DUP
5523.84	17.498(400)	17.965(400)	16.924(400)	DUP
5613.61	17.695(400)	18.098(400)	16.587(400)	DUP

[a] DUP and SWO correspond to the du Pont and Swope telescopes, respectively.

Note. — One sigma uncertainties given in parentheses are in millimag.

Table 4. UVOT far-UV Photometry of SN 2005ip and SN 2006jd

JD–2454000	Phase[a]	*uvw*2	*uvm*2	*uvw*1
		SN 2005ip		
145.51	465.9	18.267(096)	18.093(092)	17.612(081)
630.13	950.5	17.911(172)	17.777(292)	17.200(131)
786.71	1107.0	18.451(098)	18.322(103)	17.654(081)
1153.96	1474.3	19.000(150)	18.748(123)	18.202(115)
2012.26	2332.6	· · ·	· · ·	19.336(206)
		SN 2006jd		
420.77	399.7	19.179(156)	18.756(171)	18.114(115)
426.30	405.3	18.983(100)	18.767(110)	18.212(084)
452.48	431.4	18.957(097)	18.632(096)	18.132(080)
480.63	459.6	18.916(096)	18.709(108)	18.224(081)
517.09	496.0	18.860(096)	18.713(095)	18.149(081)
720.39	699.3	19.023(098)	18.969(113)	18.386(085)
809.52	788.5	19.325(116)	19.053(134)	18.648(101)

[a] Days past discovery.

Note. — One sigma uncertainties given in parentheses are in millimag.

Table 5. Spectroscopic Observations

Epoch^a	Date	Julian Date JD–2450000+	Telescope	Instrument	Range (Å)	Resolution (FWHM Å)	# of exposures	Integration (s)
				SN 2005ip				
18	2005 Nov 23	3697.8	du Pont	MS	3780 – 7289	7	3	400
19	2005 Nov 24	3698.8	du Pont	MS	3780 – 7290	7	3	600
20	2005 Nov 25	3699.8	du Pont	MS	3780 – 7289	7	3	400
20	2005 Nov 25	3699.8	CTIO60	CS	3200 – 9535	14	3	600
43	2005 Dec 18	3722.8	NTT	EMMI	4000 – 10200	8	3	300
45	2005 Dec 20	3724.8	du Pont	WFCCD	3800 – 9235	8	3	400
46	2005 Dec 21	3725.8	du Pont	WFCCD	3800 – 9208	8	3	500
48	2005 Dec 23	3727.8	du Pont	WFCCD	3800 – 9235	8	3	500
72	2006 Jan 16	3751.8	NTT	EMMI	4000 – 10200	8	3	200
80	2006 Jan 24	3759.8	Clay	LDSS	3788 – 9980	4	3	300
120	2006 Mar 05	3799.7	du Pont	WFCCD	3800 – 9235	8	3	600
130	2006 Mar 15	3809.6	NTT	EMMI	4000 – 10200	8	3	300
130	2006 Mar 15	3809.6	CLAY	LDSS	3785 – 9969	4	3	400
138	2006 Mar 23	3817.6	du Pont	WFCCD	3800 – 9235	8	3	600
169	2006 Apr 23	3848.5	du Pont	WFCCD	3800 – 9235	8	3	900
1844	2010 Nov 10	5523.7	INT	IDS	3871 – 7756	6	3	1200
2352	2012 Apr 13	6031.0	NOT	Alfosc	3675 – 8985	17	1	3600
				SN 2006jd				
22	2006 Nov 03	4042.8	NTT	EMMI	3200 – 10200	8	3	200
35	2006 Nov 16	4055.8	du Pont	WFCCD	3803 – 9235	8	3	500
41	2006 Nov 22	4061.8	du Pont	WFCCD	3800 – 9235	8	3	600
61	2006 Dec 13	4082.0	du Pont	B&C	3625 – 9832	8	3	600
67	2006 Dec 18	4087.8	du Pont	WFCCD	3800 – 9235	8	3	600
94	2007 Jan 14	4114.7	du Pont	B&C	3625 – 9835	8	3	1800
109	2007 Jan 29	4129.6	Baade	IMACS	4279 – 9538	4	3	1200
122	2007 Feb 11	4142.7	du Pont	WFCCD	3800 – 9235	8	1	1200
124	2007 Feb 13	4144.7	du Pont	WFCCD	3800 – 9235	8	3	1200
188	2007 Apr 18	4208.5	du Pont	WFCCD	3800 – 9235	8	3	1200
414	2007 Nov 30	4434.8	3.6-m	EFOSC	3300 – 9260	13	3	1200
417	2007 Dec 03	4437.8	du Pont	WFCCD	3800 – 9235	8	3	1200
423	2007 Dec 09	4443.8	du Pont	WFCCD	3800 – 9235	8	3	1200
449	2008 Jan 04	4469.7	3.6-m	EFOSC	3300 – 9260	13	3	1200
930	2009 Apr 30	4951.5	Clay	LDSS	3704 – 9424	7	3	900
1173	2009 Dec 28	5193.9	Baade	IMACS	3976 – 10050	6	1	900
1209	2010 Feb 02	5229.7	Baade	IMACS	3976 – 10050	5	3	1200
1542	2011 Jan 01	5563.0	Gemini-North	GMOS	3588 – 9653	8	1	3000

[a] Days past discovery.

Table 6. Optical Photometry of SN 2006jd in the Natural System

JD–2450000+	u	g	r	i	B	V	Telescope[a]
4028.89	···	···	···	···	18.177(061)	17.741(017)	SWO
4029.88	18.583(024)	17.881(011)	17.453(012)	17.545(027)	18.130(015)	17.745(013)	SWO
4036.88	18.646(089)	18.051(015)	···	···	18.265(024)	17.872(014)	SWO
4040.87	18.644(038)	18.051(015)	17.638(014)	···	18.274(014)	17.892(014)	SWO
4042.86	···	18.038(012)	17.658(014)	17.799(016)	···	···	SWO
4046.82	18.666(061)	18.061(016)	17.697(013)	17.799(016)	18.309(025)	17.947(017)	SWO
4066.86	···	18.226(015)	17.963(015)	18.111(032)	18.457(017)	18.146(019)	SWO
4071.76	18.967(042)	18.270(013)	18.019(016)	18.110(019)	18.497(019)	18.205(018)	SWO
4076.81	18.980(069)	18.280(017)	18.107(018)	18.166(020)	18.538(026)	18.233(020)	SWO
4085.79	18.971(028)	18.333(014)	18.174(019)	18.273(022)	18.566(014)	18.299(017)	SWO
4087.83	18.983(024)	18.363(018)	18.195(021)	18.277(024)	18.600(017)	18.325(022)	SWO
4092.81	19.053(030)	18.416(019)	18.253(023)	18.341(026)	18.639(018)	18.383(024)	SWO
4096.77	···	18.446(018)	18.282(022)	18.347(022)	···	···	SWO
4099.77	19.051(028)	18.463(016)	18.362(019)	18.382(027)	18.692(018)	18.471(023)	SWO
4102.74	···	18.530(023)	18.393(027)	18.472(025)	18.784(035)	18.533(031)	SWO
4105.80	···	18.545(024)	18.380(025)	18.485(030)	18.780(029)	18.481(023)	SWO
4110.76	···	18.540(015)	18.423(019)	18.506(024)	18.748(016)	18.523(017)	SWO
4112.77	···	18.568(017)	18.448(021)	18.505(025)	18.802(016)	18.537(019)	SWO
4119.74	···	18.554(015)	18.407(021)	18.491(028)	18.759(024)	18.525(021)	SWO
4121.74	···	18.571(017)	18.447(020)	18.573(027)	18.841(017)	18.523(021)	SWO
4125.72	···	18.615(020)	18.501(026)	18.623(027)	18.850(017)	18.598(022)	SWO
4130.65	···	18.698(017)	18.599(021)	18.699(028)	18.902(022)	18.693(024)	SWO
4133.71	···	18.724(031)	18.608(033)	18.667(036)	18.884(043)	18.669(038)	SWO
4136.74	···	18.720(017)	18.622(020)	18.751(032)	18.931(022)	18.730(021)	SWO
4143.69	···	18.704(025)	18.582(033)	18.744(033)	18.946(023)	18.725(025)	SWO
4163.67	···	18.818(023)	18.687(025)	18.861(028)	18.995(039)	18.841(028)	SWO
4170.61	19.288(024)	18.788(023)	18.655(030)	18.857(035)	18.995(020)	18.798(027)	SWO
4190.56	19.391(053)	18.872(019)	18.695(021)	18.916(029)	19.051(024)	18.945(022)	SWO
4225.53	19.217(065)	18.868(022)	···	···	19.009(031)	18.896(024)	SWO
4383.84	···	18.858(020)	18.011(013)	18.879(038)	19.047(018)	18.821(024)	SWO
4392.88	···	···	18.004(014)	19.061(035)	···	···	SWO
4394.84	···	18.905(023)	17.995(019)	19.061(035)	19.122(024)	18.921(027)	SWO
4400.80	···	18.835(033)	17.943(014)	18.877(051)	19.070(055)	18.854(065)	SWO
4411.83	···	18.875(025)	17.948(017)	19.051(033)	19.108(022)	18.892(029)	SWO
4413.86	···	18.835(019)	17.925(012)	18.956(050)	19.027(020)	18.804(025)	SWO
4417.77	···	18.876(022)	17.925(017)	19.034(035)	···	18.902(031)	SWO
4421.75	···	18.893(021)	17.912(016)	18.989(036)	19.129(024)	18.898(030)	SWO
4435.78	···	18.829(018)	17.850(012)	18.925(036)	19.075(020)	18.825(024)	SWO
4440.78	···	18.863(029)	17.844(022)	18.984(037)	19.083(026)	18.868(029)	SWO
4445.77	···	18.837(032)	17.826(021)	19.023(035)	19.107(022)	18.864(032)	SWO
4447.74	19.295(026)	18.831(026)	17.823(015)	18.941(033)	19.083(023)	18.850(029)	SWO
4453.77	···	18.838(026)	17.802(018)	18.986(036)	19.091(021)	18.854(027)	SWO
4455.72	···	18.841(022)	17.822(011)	19.005(034)	19.101(022)	18.904(023)	SWO
4457.76	···	18.868(024)	17.824(012)	18.918(033)	19.096(031)	18.905(029)	SWO
4464.72	···	18.892(023)	17.798(020)	19.025(037)	19.133(020)	18.888(024)	SWO

Table 6—Continued

JD–2450000+	u	g	r	i	B	V	Telescope[a]
4466.76	···	18.878(023)	17.788(018)	18.978(037)	19.131(020)	18.875(026)	SWO
4469.67	···	18.809(020)	17.784(013)	18.948(033)	19.055(017)	18.791(024)	SWO
4470.70	···	18.839(023)	17.784(014)	18.989(036)	19.109(022)	18.871(030)	SWO
4480.70	···	18.874(020)	17.782(015)	19.059(038)	19.156(021)	18.865(027)	SWO
4484.64	···	18.929(017)	17.776(011)	18.991(032)	19.120(027)	18.912(025)	SWO
4488.68	···	18.985(037)	17.759(014)	19.037(050)	19.176(059)	18.998(045)	SWO
4492.74	···	···	17.768(012)	18.991(036)	19.204(126)	18.896(022)	SWO
4512.65	···	···	17.721(012)	19.058(048)	···	18.913(064)	SWO
4521.65	···	···	17.725(014)	19.055(035)	···	18.904(024)	SWO
4523.60	···	···	17.705(017)	19.059(039)	···	18.885(025)	SWO
4540.64	···	···	17.736(018)	19.209(037)	···	19.003(024)	DUP
4549.54	···	···	17.706(014)	19.119(036)	···	···	SWO
4564.51	···	···	17.684(013)	19.040(038)	···	···	SWO
4575.55	···	···	17.726(014)	19.182(037)	···	···	SWO
4591.49	···	···	17.727(021)	19.196(043)	···	···	SWO
4774.31	19.876(030)	19.194(019)	17.848(044)	19.783(040)	19.600(020)	19.163(037)	DUP
5268.21	21.499(067)	21.009(061)	19.416(033)	21.088(085)	21.405(059)	20.921(067)	DUP
5659.29	22.013(080)	21.524(072)	···	···	21.721(071)	21.492(088)	DUP

[a] DUP and SWO correspond to the du Pont and Swope telescopes, respectively.

Note. — One sigma uncertainties given in parentheses are in millimag.

Table 7. Near-infrared Photometry of SN 2006jd

JD–2450000+	Y	J	H	K_s	Telescope[a]
4041.84	16.711(024)	16.753(043)	16.021(039)	· · ·	SWO
4043.80	16.779(036)	16.752(052)	16.012(053)	· · ·	SWO
4047.83	16.738(031)	16.624(042)	· · ·	· · ·	SWO
4053.86	16.789(022)	16.641(036)	15.925(037)	· · ·	SWO
4057.77	16.763(033)	16.567(039)	15.890(035)	· · ·	SWO
4066.85	16.854(021)	16.669(021)	· · ·	· · ·	DUP
4072.76	16.853(019)	16.565(027)	15.645(025)	· · ·	SWO
4077.80	16.903(019)	16.558(031)	15.646(022)	· · ·	SWO
4082.84	16.922(019)	16.596(034)	15.615(025)	· · ·	SWO
4086.82	16.936(021)	16.550(027)	15.612(028)	· · ·	SWO
4093.76	16.981(036)	16.523(031)	15.653(038)	· · ·	SWO
4100.75	17.073(024)	16.684(021)	15.625(021)	· · ·	DUP
4107.76	17.114(030)	16.563(027)	15.577(029)	· · ·	SWO
4109.82	17.148(026)	16.621(028)	· · ·	· · ·	SWO
4114.74	17.149(023)	16.756(039)	15.604(029)	· · ·	SWO
4120.72	17.188(025)	16.644(024)	15.569(018)	· · ·	SWO
4122.75	17.189(022)	16.688(024)	15.636(023)	· · ·	SWO
4124.73	17.192(025)	16.662(030)	15.546(025)	· · ·	SWO
4126.67	17.206(028)	16.699(033)	15.604(029)	· · ·	SWO
4129.65	17.238(025)	16.696(026)	15.639(021)	· · ·	SWO
4135.65	17.257(026)	16.741(025)	15.622(024)	· · ·	SWO
4138.63	17.275(027)	16.652(034)	15.633(023)	· · ·	SWO
4140.61	17.245(030)	16.727(032)	15.620(027)	· · ·	SWO
4146.64	17.308(030)	16.729(028)	15.595(027)	· · ·	SWO
4150.63	17.332(027)	16.724(031)	15.602(024)	· · ·	SWO
4158.66	17.380(021)	16.887(021)	15.687(015)	14.584(021)	DUP
4162.61	17.345(037)	16.803(041)	15.651(035)	· · ·	SWO
4164.64	17.344(031)	16.771(031)	15.669(024)	· · ·	SWO
4169.58	17.413(021)	16.915(021)	15.709(021)	14.559(021)	DUP
4175.55	17.353(029)	16.881(046)	15.627(028)	· · ·	SWO
4189.56	17.446(046)	16.823(041)	15.684(042)	· · ·	SWO
4198.51	17.441(036)	16.755(052)	15.660(034)	· · ·	SWO
4220.48	17.463(047)	16.915(063)	15.672(040)	· · ·	SWO
4234.47	17.322(081)	16.817(074)	15.616(054)	· · ·	SWO
4247.46	17.466(054)	16.704(056)	15.551(054)	· · ·	SWO
4384.86	17.319(030)	16.775(034)	15.507(021)	· · ·	SWO
4393.85	17.325(034)	16.791(037)	15.555(021)	· · ·	SWO
4396.87	17.354(027)	16.731(030)	15.559(026)	· · ·	SWO
4408.85	17.326(034)	16.783(038)	15.542(033)	· · ·	SWO
4416.83	17.372(025)	16.806(027)	15.532(020)	· · ·	SWO
4424.84	17.330(028)	16.780(032)	15.560(025)	· · ·	SWO
4431.81	17.311(032)	16.792(041)	15.528(046)	· · ·	SWO
4432.75	17.326(032)	16.743(028)	15.544(038)	· · ·	SWO
4437.79	17.298(024)	16.745(028)	15.519(029)	· · ·	SWO
4439.78	17.330(021)	16.768(028)	15.505(029)	· · ·	SWO
4446.86	17.288(021)	16.753(024)	· · ·	· · ·	SWO

Table 7—Continued

JD–2450000+	Y	J	H	K_s	Telescope[a]
4454.73	17.282(024)	16.761(023)	15.501(022)	···	SWO
4465.76	17.246(019)	16.753(018)	15.514(016)	···	SWO
4473.78	17.289(026)	16.737(026)	15.479(015)	···	SWO
4487.75	17.314(023)	16.741(030)	15.482(016)	···	SWO
4498.73	17.289(020)	16.751(020)	15.496(015)	···	SWO
4513.70	17.359(057)	16.780(049)	15.512(021)	···	SWO
4530.65	17.315(021)	16.785(024)	15.511(023)	···	SWO
4536.62	17.292(023)	16.742(027)	15.550(021)	···	SWO
4544.64	17.331(022)	16.843(024)	15.574(027)	···	SWO
4550.63	17.320(027)	16.872(028)	···	···	SWO
4627.50	17.490(025)	17.140(040)	···	···	SWO
4841.65	···	···	16.441(021)	···	DUP
4954.84	18.527(056)	18.348(074)	16.725(051)	14.955(021)	SWO
5133.30	18.900(060)	18.968(079)	17.324(039)	15.358(030)	DUP
5194.76	19.085(055)	19.119(075)	17.508(030)	15.512(023)	DUP
5260.57	19.012(052)	19.321(092)	17.734(037)	15.673(026)	DUP
5314.50	19.145(067)	19.440(106)	17.829(065)	···	DUP
5521.50	19.453(062)	19.611(121)	18.273(067)	16.194(025)	DUP
5613.72	19.396(083)	19.749(117)	18.510(096)	16.433(043)	DUP

[a] DUP and SWO correspond to the du Pont and Swope telescopes, respectively.

Note. — One sigma uncertainties given in parentheses are in millimag.

Table 8. Physical Parameters of BB fits

Epoch^a (days)	T_w (K)	$\log_{10}(L_w)$ (erg s^{-1})	R_w (10^{16} cm)	T_h (K)	$\log_{10}(L_h)$ (erg s^{-1})	R_h (10^{14} cm)	L_{hot}/L_{tot} (percent)
			SN 2005ip				
10	···	···	···	6484	42.485	15.58	···
58	1413	41.444	0.989	6704	42.100	9.353	82
99	1596	41.775	1.135	7146	41.680	5.073	45
211	1544	41.794	1.240	6613	41.363	4.115	27
722	1233	41.743	1.834	7123	41.233	3.053	24
1565	969	41.781	3.101	6565	40.965	2.639	13
			SN 2006jd				
9	1194	41.938	2.447	6999	42.355	10.51	72
51	1478	42.148	2.034	7353	42.180	8.523	57
99	1562	42.210	1.955	8097	42.221	6.165	42
204	1515	42.245	2.165	9307	41.969	4.176	35
753	1157	42.333	4.106	8018	41.766	4.450	21
1638	980	41.747	2.917	8479	40.881	1.437	12

[a] Days past discovery.

Table 9. Warm Dust Mass Estimates

Days Past Discovery	M$_d$($10^{-4} M_\odot$) $a = 1\ \mu m$	M$_d$($10^{-4} M_\odot$) $a = 0.1\ \mu m$	M$_d$($10^{-4} M_\odot$) $a = 0.01\ \mu m$
	SN 2005ip		
10	⋯	⋯	⋯
58	0.20	0.45	0.53
99	0.26	0.62	0.71
211	0.32	0.83	0.93
722	0.72	1.88	2.09
1565	2.05	5.41	6.00
	SN 2006jd		
9	1.02	2.88	3.32
51	0.72	1.66	2.04
99	0.67	1.60	1.93
204	0.80	2.40	2.71
753	2.86	8.72	9.84
1638	1.44	4.62	5.14

Table 10. Pre-Existing Dust Masses and BB_c Physical Parameters

SN	Days Past Discovery	M_d ($M_\odot$)	R (10^{16}cm)	T (K)
2005ip	930	0.01	5.14	502
2006jd	1150	0.02	8.47	726
2006jd	1638	0.02	9.28	578

Note. — Best-fit values for graphite composition with grain size of 0.1 μm.

Table 11. Fluxes of Lines Indicated in Figure 12

ID	λ (Å)	Flux d22 (10^{-16} erg s^{-1} cm^{-2})	Flux d1542 (10^{-16} erg s^{-1} cm^{-2})
[Ne III]	3869	21.70	2.40
[Ne III]	3967	5.47	1.96
Hδ	4102	···	1.57
Hγ	4340	···	1.00
[O III]	4363	11.60	1.53
Hβ	4861	6.82	0.95
[O III]	4959	10.30	0.79
[O III]	5007	23.90	2.68
[Fe VII]	5159	···	0.45
[Fe VII]	5276 +[Fe VI]	···	0.38
[Ar X]	5533	···	0.46
[Fe VII]	5721	···	0.63
[N II]	5755	9.09	1.39
He I	5876	1.22	2.66
[Fe VII]	6087	···	0.55
[O I]	6300	···	0.41
[Si III]	6312	···	0.15
[O I]	6364	···	0.27
[Fe X]	6375	···	0.57
Hα	6563	86.15	···
[S II]	6717/31	···	0.31/0.12
He I	7065	6.79	0.54
[Ar III]	7136	···	0.30
[Fe II]	7155	···	0.36
[O II]	7325	···	0.19
[Fe XI]	7892	···	0.35
He I	8156	···	0.09
[Cr II]	8230	···	0.14

Note. — Fluxes of Lines Indicated in Figure 12.

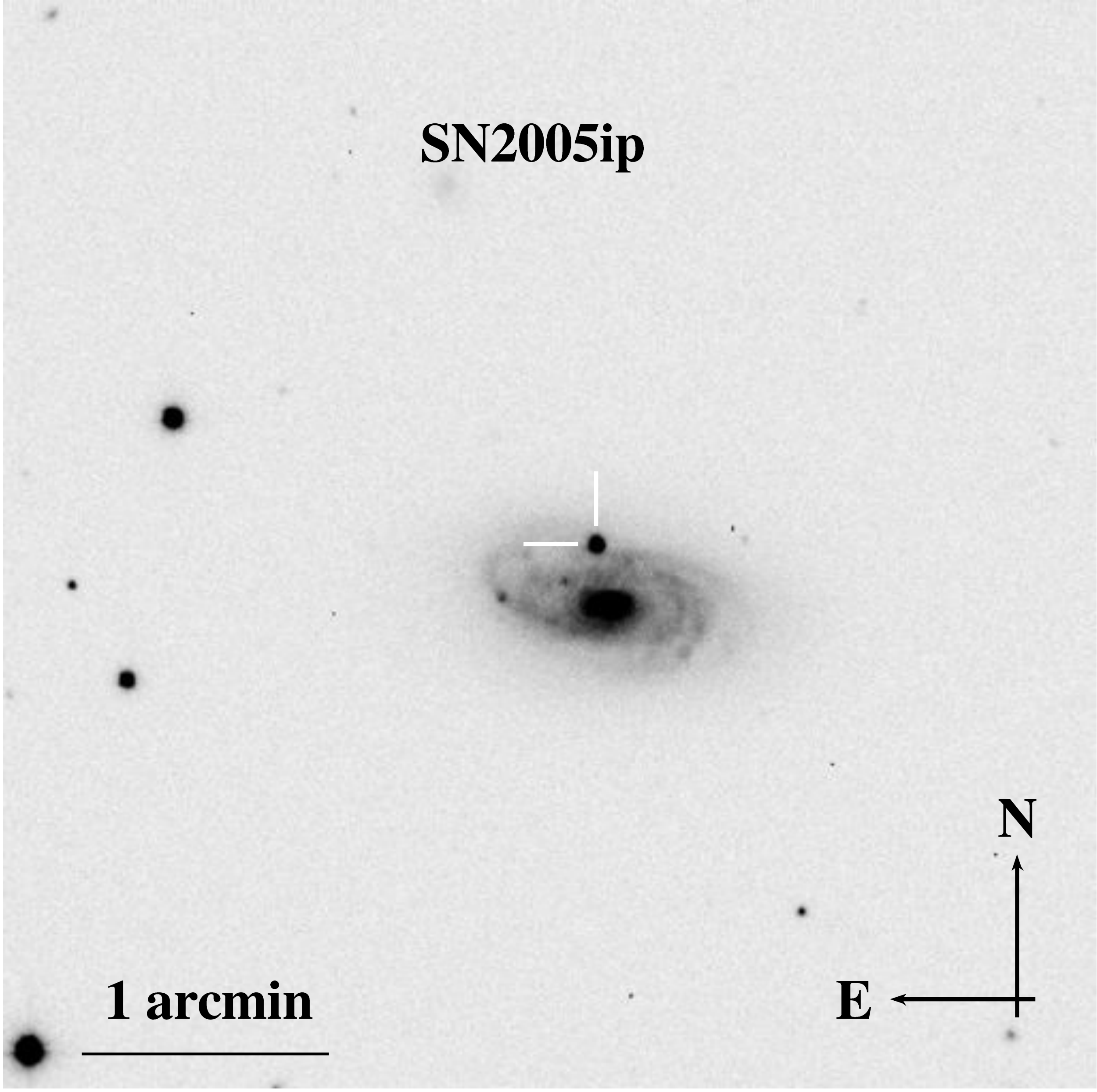

Fig. 1.— Swope V-band image of NGC 2906 with SN 2005ip indicated.

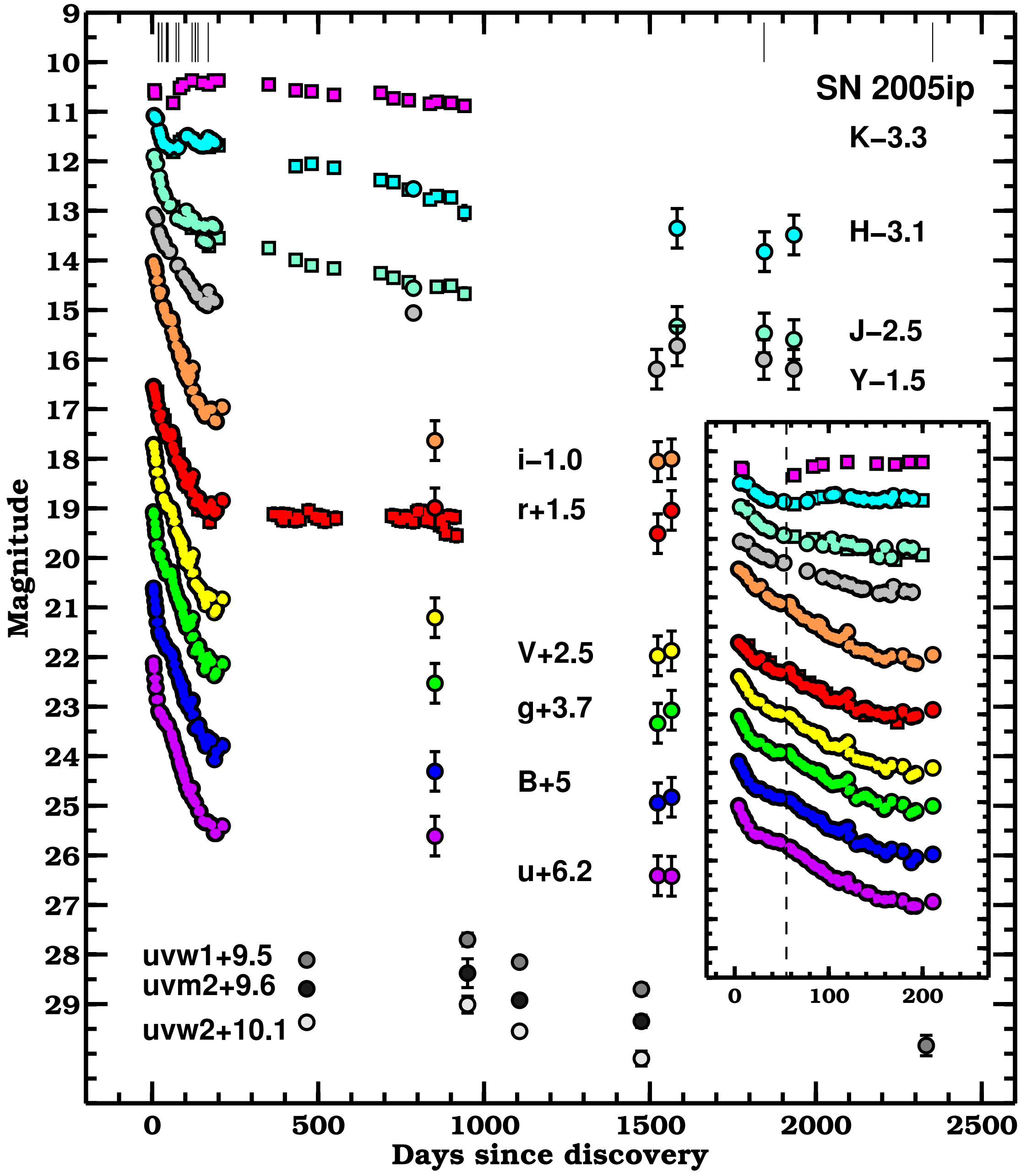

Fig. 2.— UV, optical and near-IR light curves of SN 2005ip (filled dots), and published unfiltered (Smith et al. 2009) and near-IR (Fox et al. 2009) photometry (filled squares). Contained within the inset is the photometric evolution over the first ~ 200 days, with the vertical dashed line marking the time when the optical light curves begin to drop at an increased rate. Simultaneously, the H- and K_s-band light curves show an excess in emission. These transitions are related to dust condensation (see text). Vertical lines at the top of the figure indicate the epochs in which spectra where obtained (see Table 5).

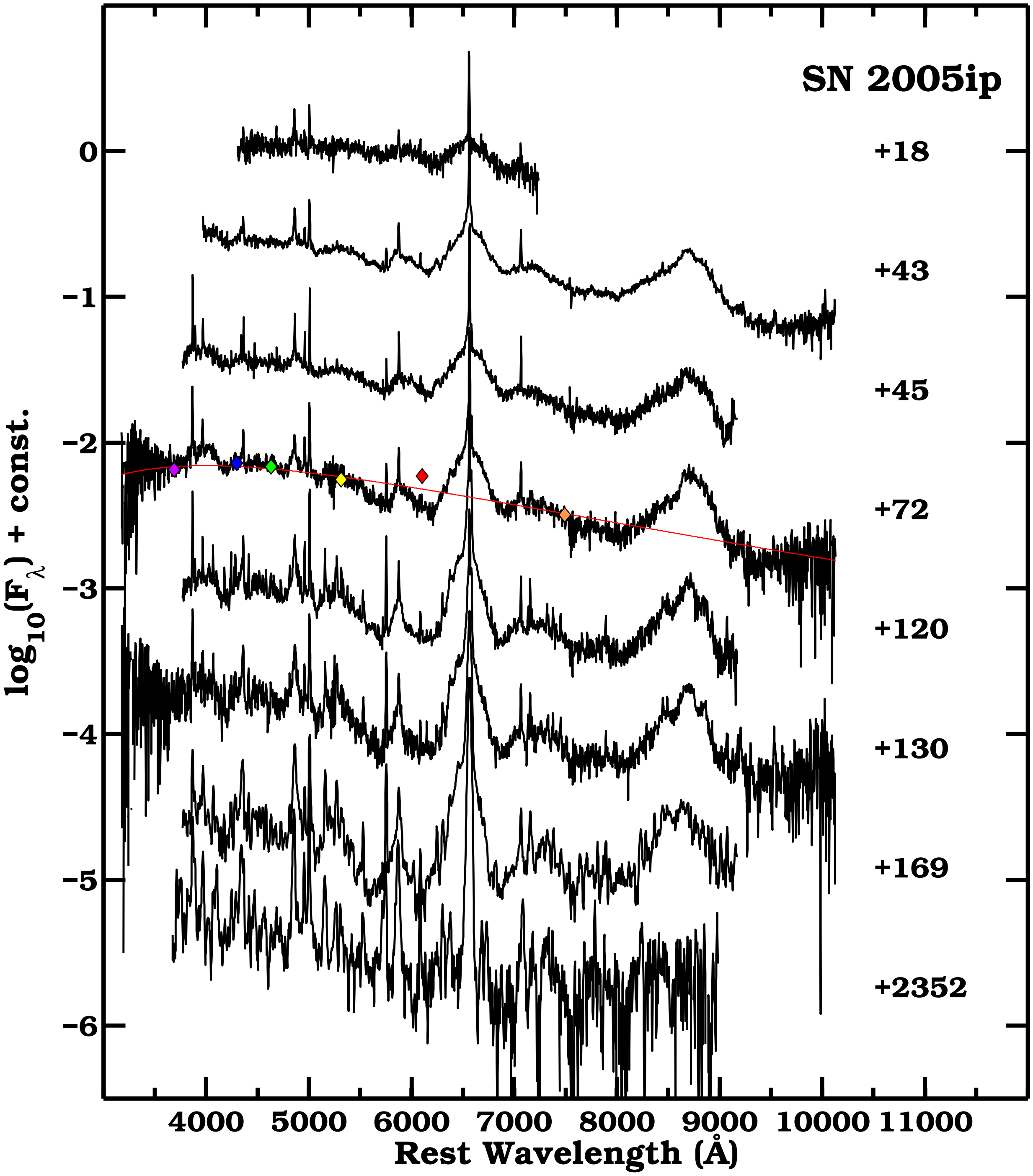

Fig. 3.— A subset of our spectroscopic sequence of SN 2005ip from 18 to 2352 days past discovery. Over-plotted the day 72 spectrum is the hot BB_h component derived from fits to the $uBgVi$ broad-band flux points (see Section 3.3).

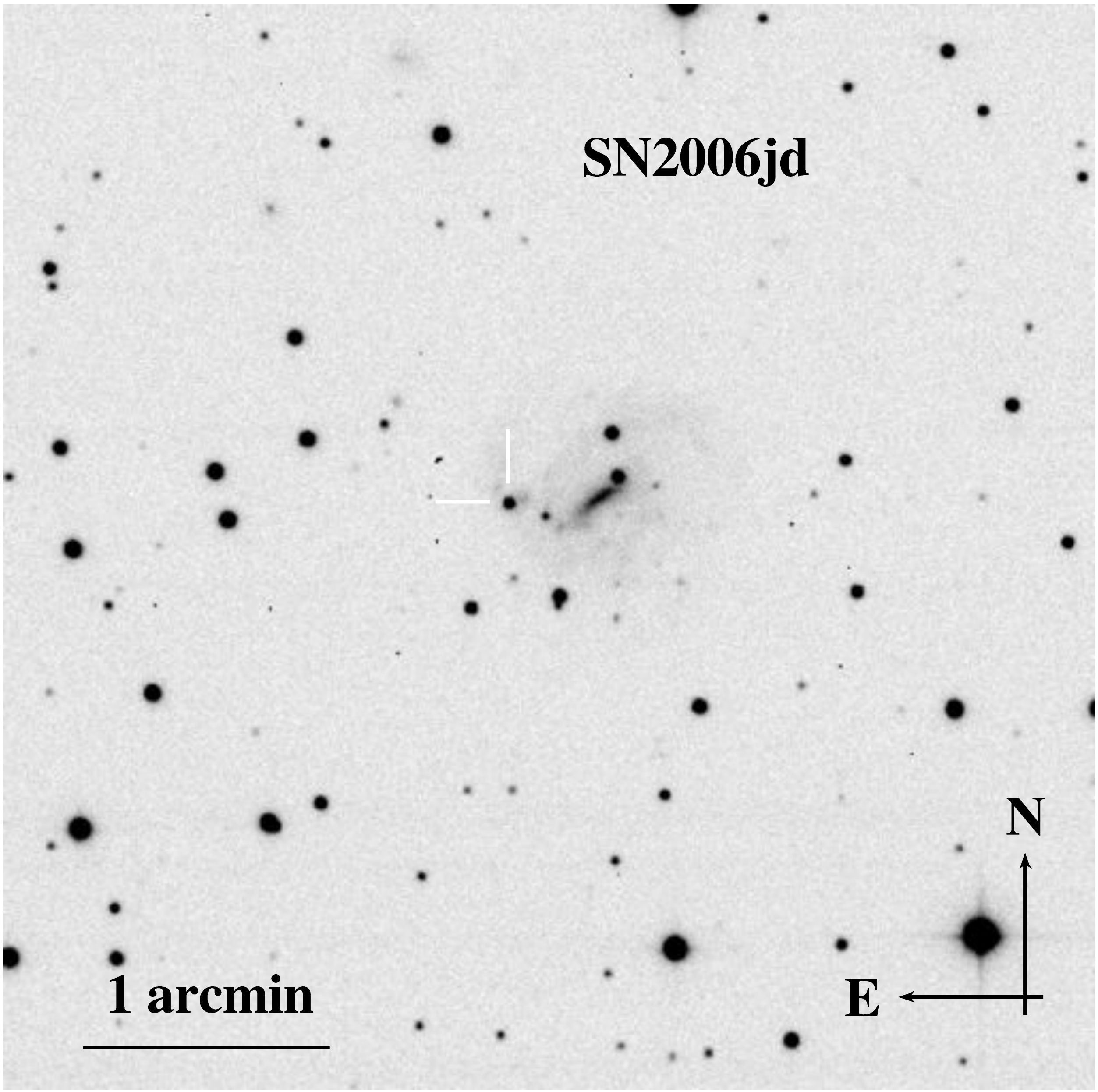

Fig. 4.— Swope V-band image of UGC 4179 with SN 2006jd indicated.

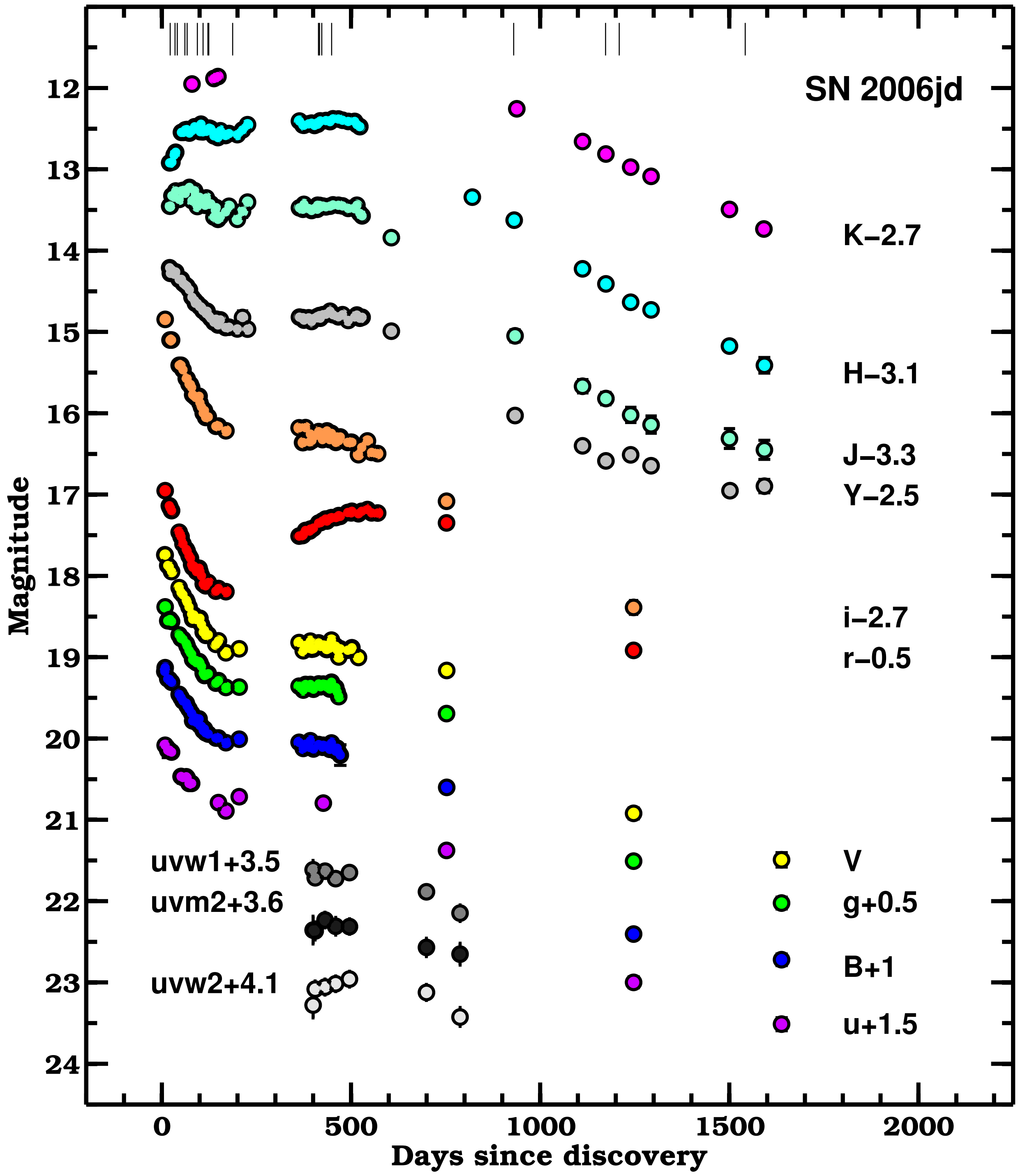

Fig. 5.— UV, optical and near-IR light curves of SN 2006jd. Vertical lines at the top of the figure mark the epochs in which spectroscopy has been obtained.

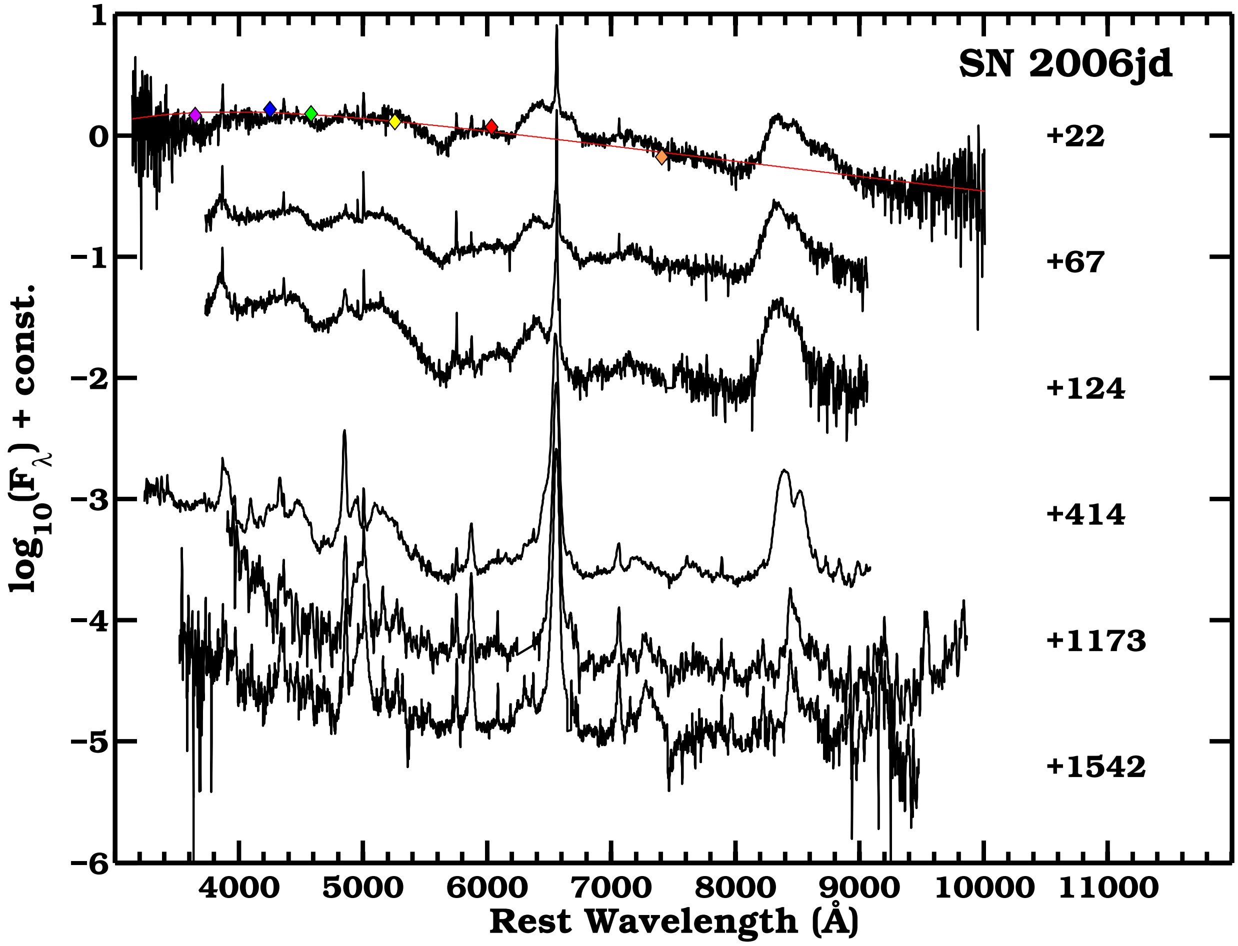

Fig. 6.— A subset of our spectroscopic sequence of SN 2006jd from 22 to 1542 days past discovery. Over-plotted the day 22 spectrum is the hot BB_h component derived from fits to the $uBgVi$ broad-band flux points.

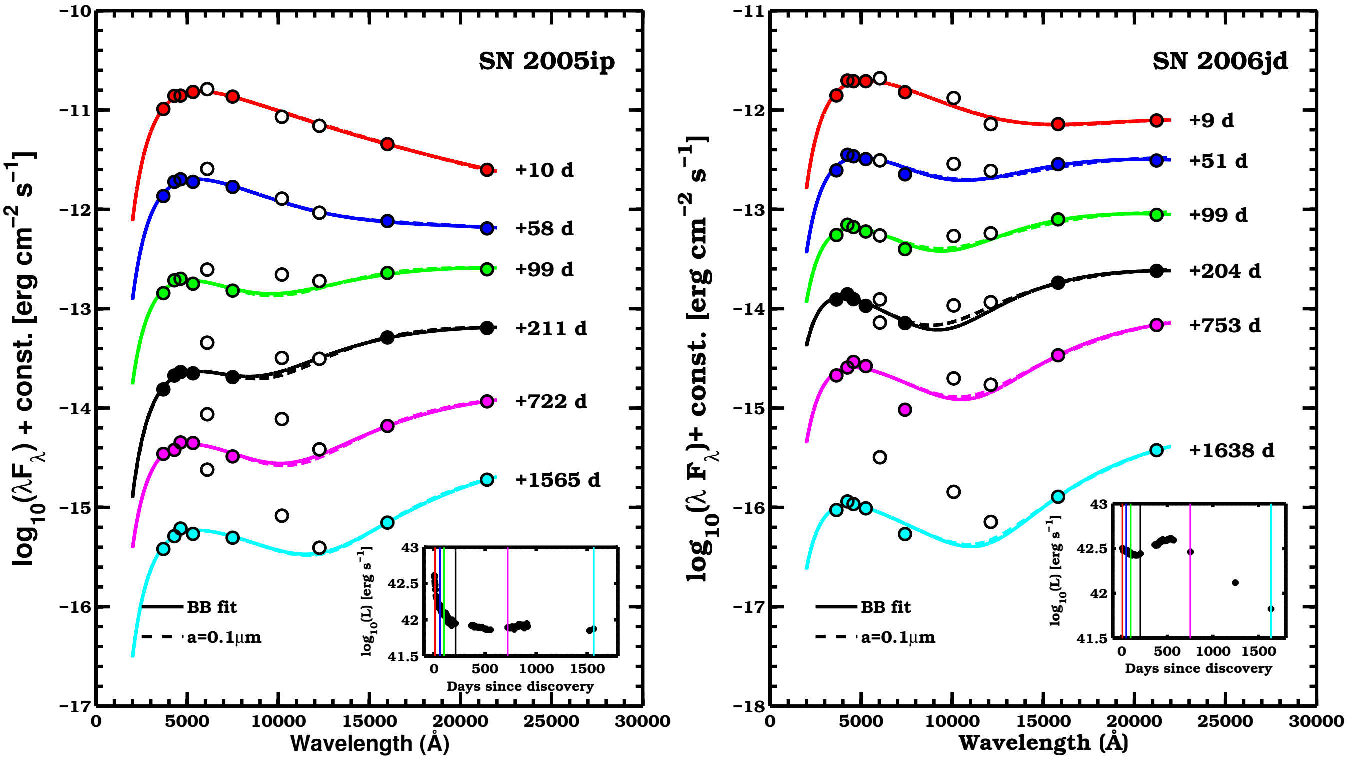

Fig. 7.— SEDs of SN 2005ip *(left)* and SN 2006jd *(right)* at six epochs constructed from broad-band optical ($uBgVri$) and near-IR ($YJHK_s$) photometry. Insets indicate the phase of the plotted SEDs with respect to the quasi-bolometric light curve. White filled circles correspond to the rYJ flux points which are excluded from the BB fits due to strong emission-line contamination. Solid lines correspond to two-component $BB_{h,w}$ fits to the optical and near-IR flux points, while the dashed lines correspond to modified dust mass $BB_{h,w}$ functions. Note that the Rayleigh-Jeans tail of the BB_w component is not included in the figure.

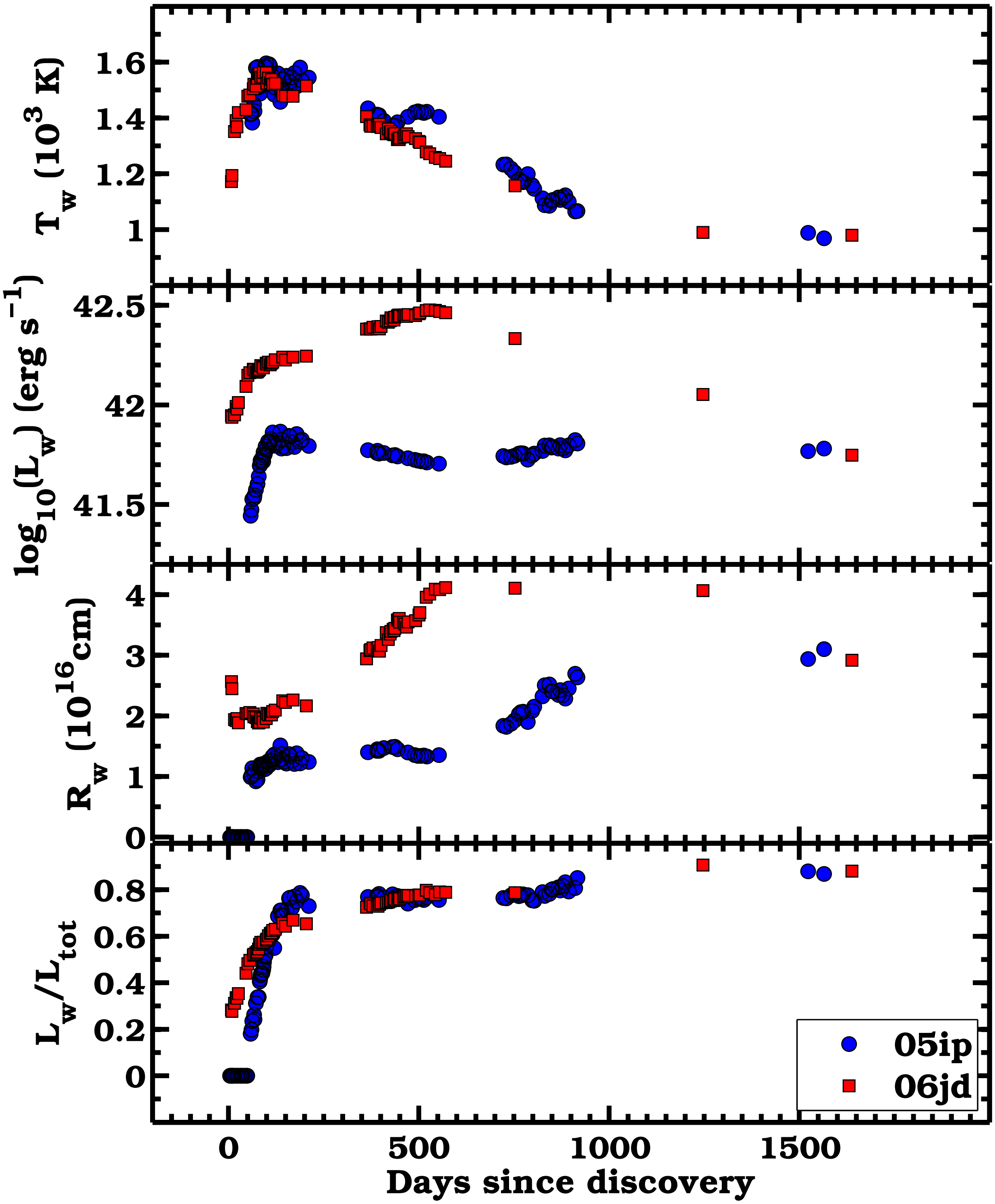

Fig. 8.— Evolution of the physical parameters: temperature, luminosity and radius derived from the "warm" BB_w component fit to the H- and K_s-band photometry of SNe 2005ip (filled blue dots) and 2006jd (filled red squares). Also shown in the bottom panel is the ratio of the warm BB_w luminosity to the total luminosity.

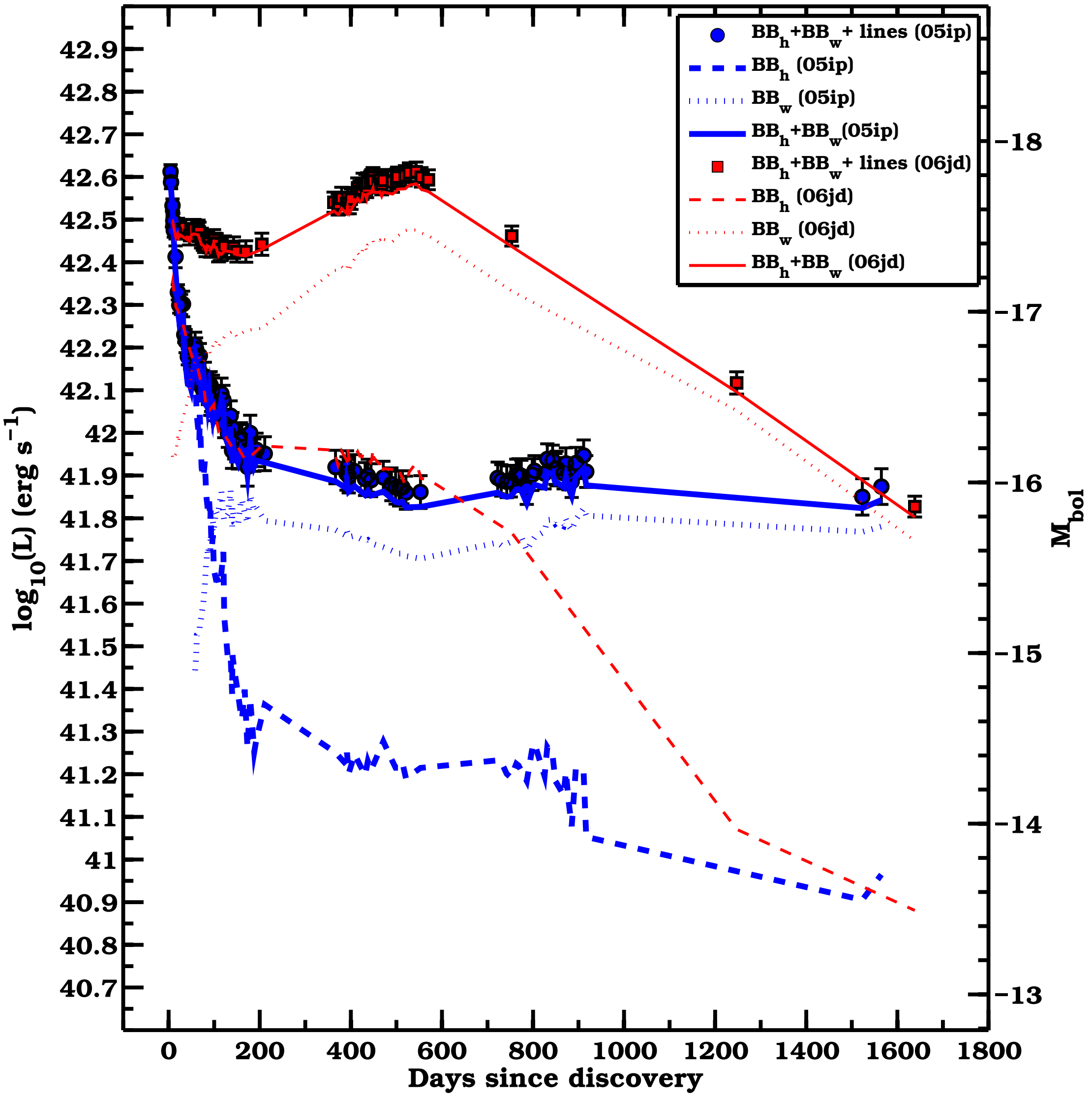

Fig. 9.— Quasi-bolometric light curves of SNe 2005ip and 2006jd plotted as points. Also included are the BB_h (dashed lines) and BB_w (dotted lines) components, and the summation of the two (solid lines). For clarity the three curves corresponding to SN 2005ip are drawn extra thick.

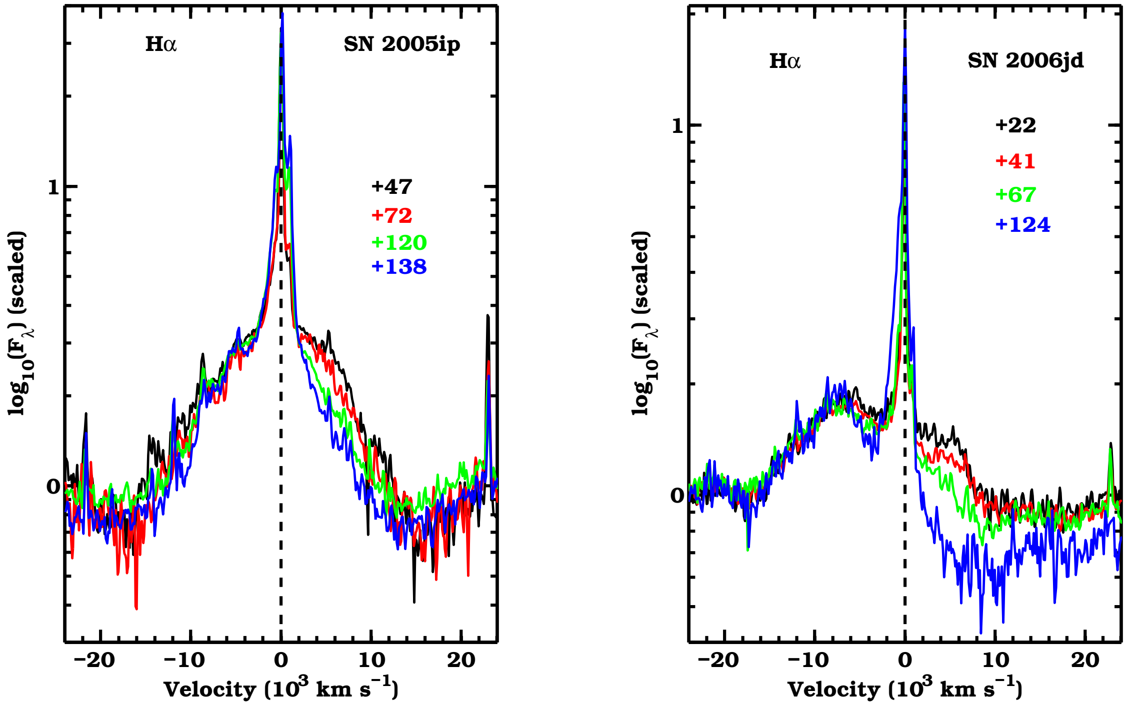

Fig. 10.— Hα line-profile evolution of SNe 2005ip and 2006jd covering the initial four months of the linear decline phase. The spectra have been scaled and superposed on top of each other. Note in SN 2006jd the broad component is asymmetric, showing an excess of flux in the blue, while the suppression of the red wing over time is clearly more extreme than in SN 2005ip.

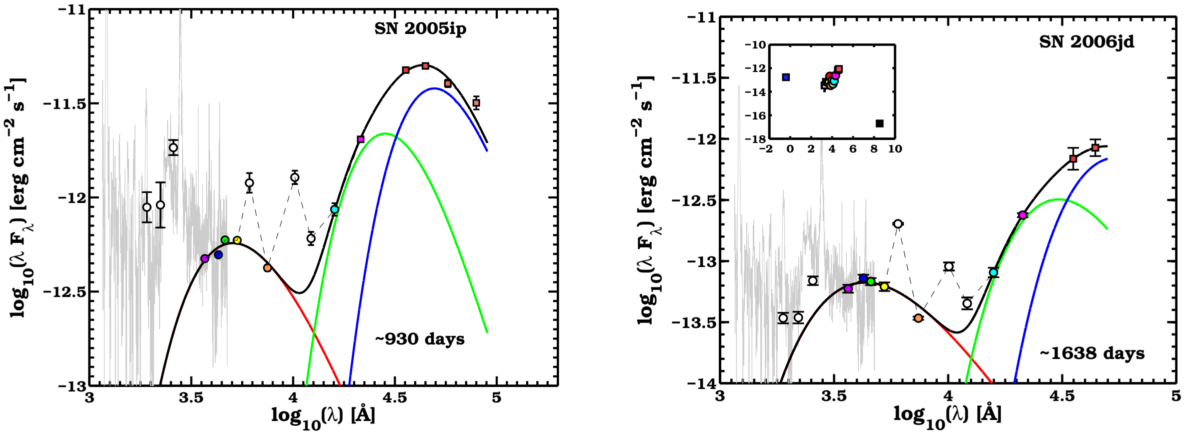

Fig. 11.— Full SED of SN 2005ip (*left*) on day $\sim$ 930 and SN 2006jd (*right*) on day $\sim$ 1638. The SEDs of both objects extends from the UV to the mid-IR. The inset contained within the plot of SN 2006jd also includes X-ray and radio measurements. White filled circles correspond to the UV- and rYJ-band flux points which were excluded from the BB fits. Also plotted in each panel is a late phase ($\sim$ 1000 days past explosion) HST spectrum of the 1988Z-like SN 1995N (Fransson et al. 2002) scaled to match the ground-based u- and B-band flux points. Black solid lines correspond to the combined three-component BB fit, while the red, green and blue lines correspond to the individual hot, warm and cold components.

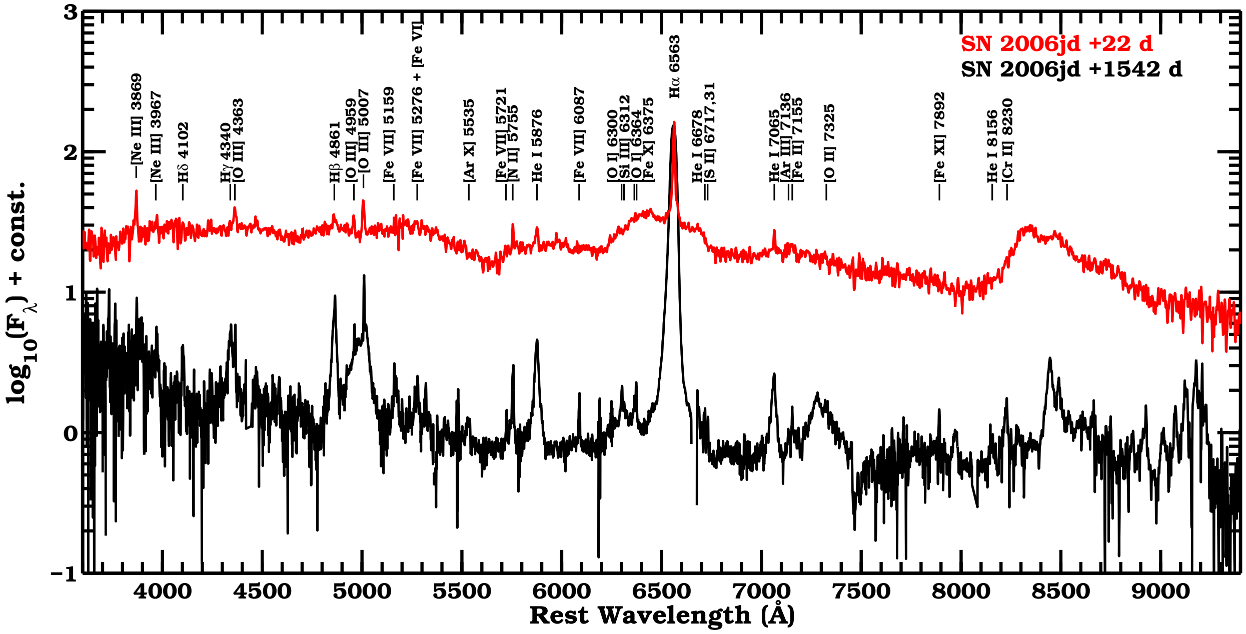

Fig. 12.— Comparison of the day 22 and day 1542 spectra of SN 2006jd. Ions responsible for many of the features are indicated. Features of [O III] $\lambda\lambda$4959, 5007, He I $\lambda\lambda$5876, 7065 and Hα all exhibit prominent intermediate-width components in the day 1542 spectrum, which are associated with post-shock gas.

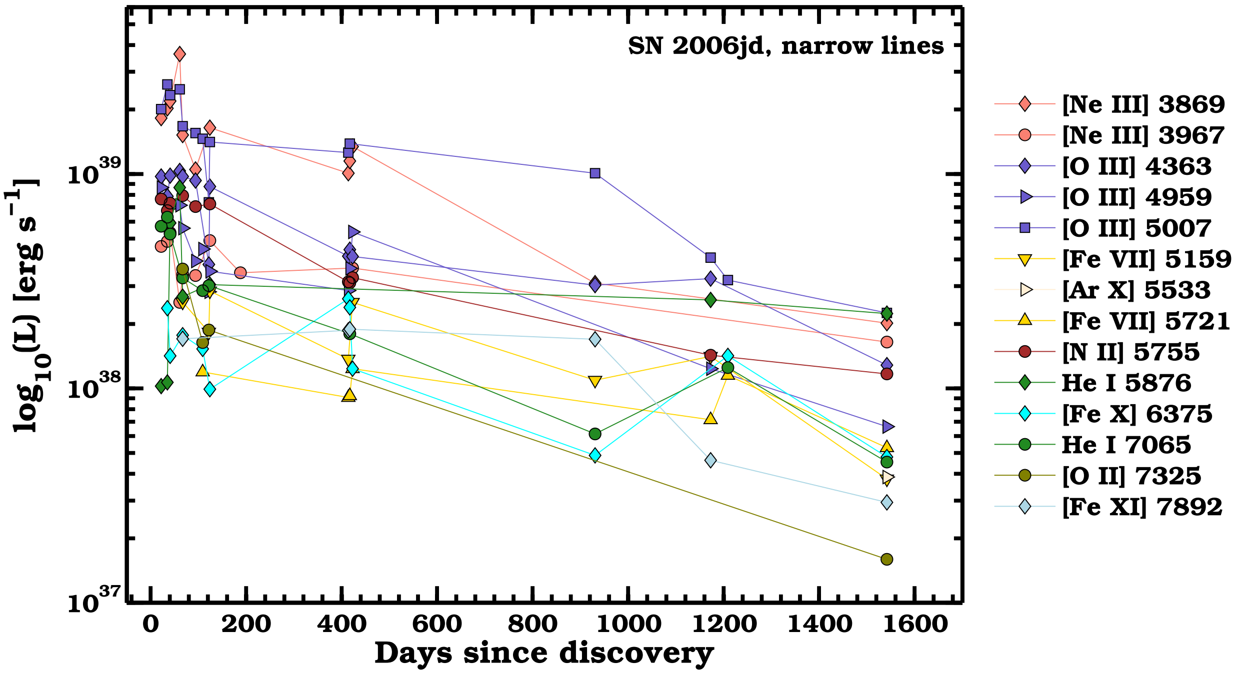

Fig. 13.— Luminosity evolution of forbidden and He I $\lambda\lambda$5876, 7065 emission lines measured from the spectroscopic sequence of SN 2006jd.

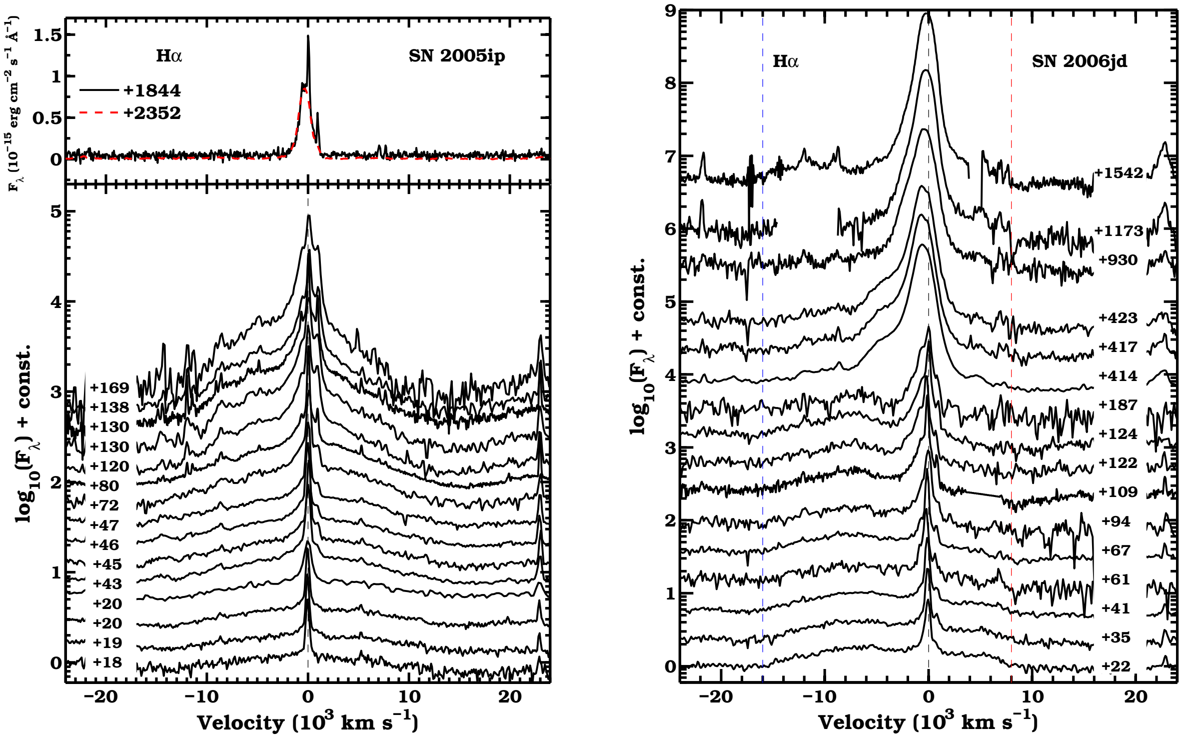

Fig. 14.— Hα line profile evolution as observed from our spectroscopic time-series of SN 2005ip *(left panel)* and SN 2006jd *(right panel)*. The epoch of each spectrum with respect to the date of discovery is indicated. In the case of SN 2005ip the two late phase spectra are plotted on top of one another, while in the plot of SN 2006jd, vertical lines highlight the asymmetric nature of the broad component.

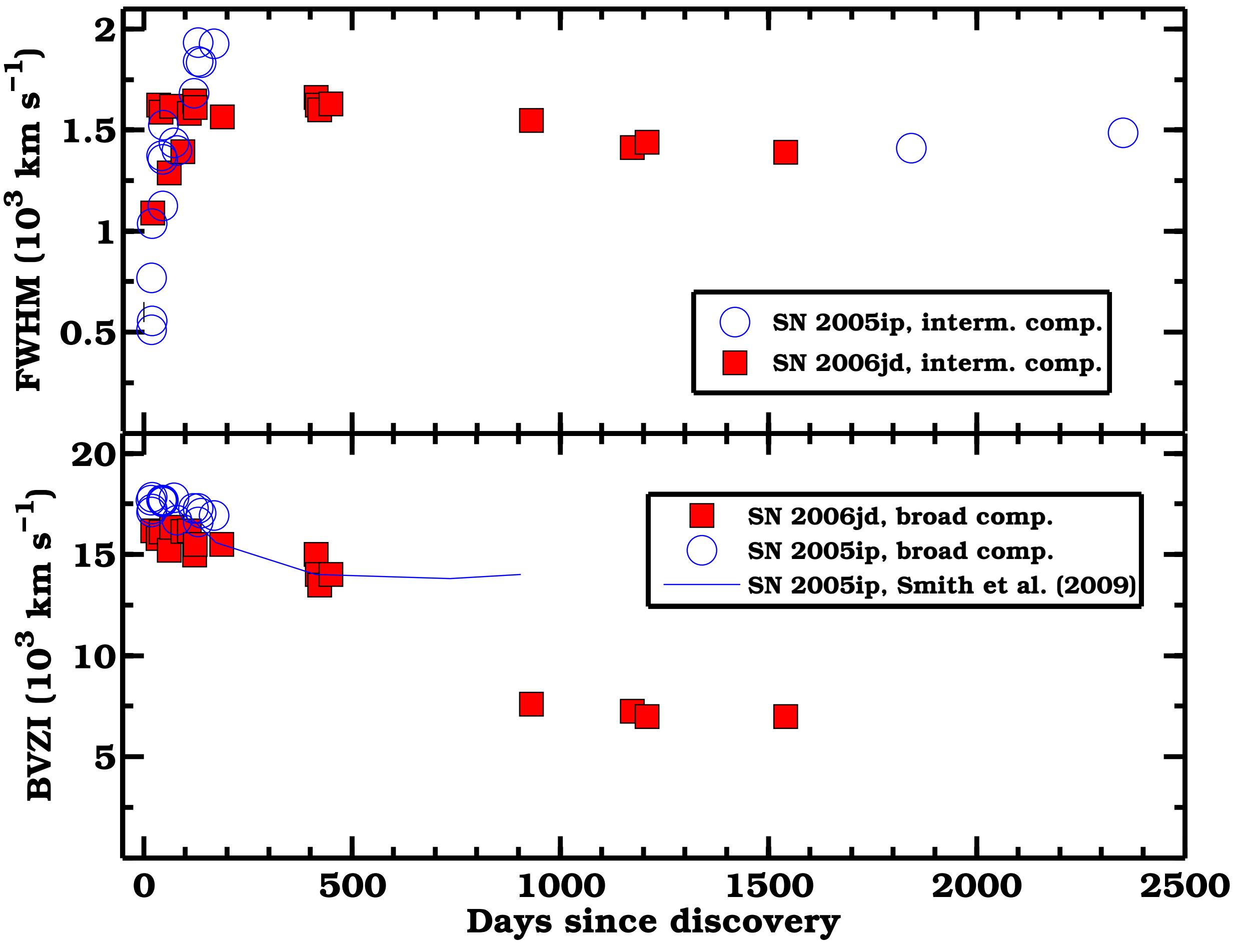

Fig. 15.— Evolution of the width of the Hα profile over time. Top panel displays the FWHM velocity of SNe 2005ip and 2006jd obtained from Gaussian fits to the intermediate-width component. Bottom panel shows the evolution of BVZI (blue-velocity at zero intensity) of the broad Hα component, including the values measured from Smith et al. (2009) for SN 2005ip out to $\sim$ 900 days.

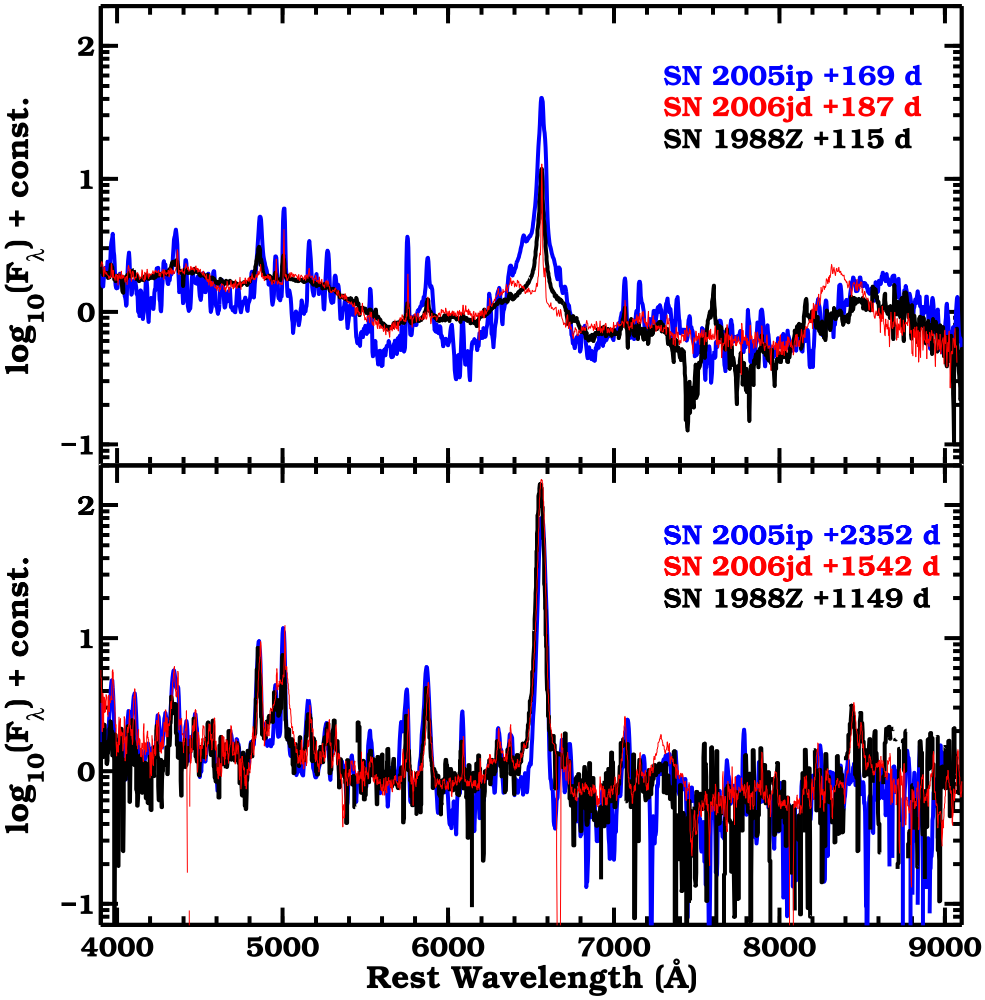

Fig. 16.— Comparison of early (top) and late (bottom) phase spectra of SNe 1988Z, 2005ip and 2006jd. Date provided next to the label of each SN spectrum refers to epoch past discovery.

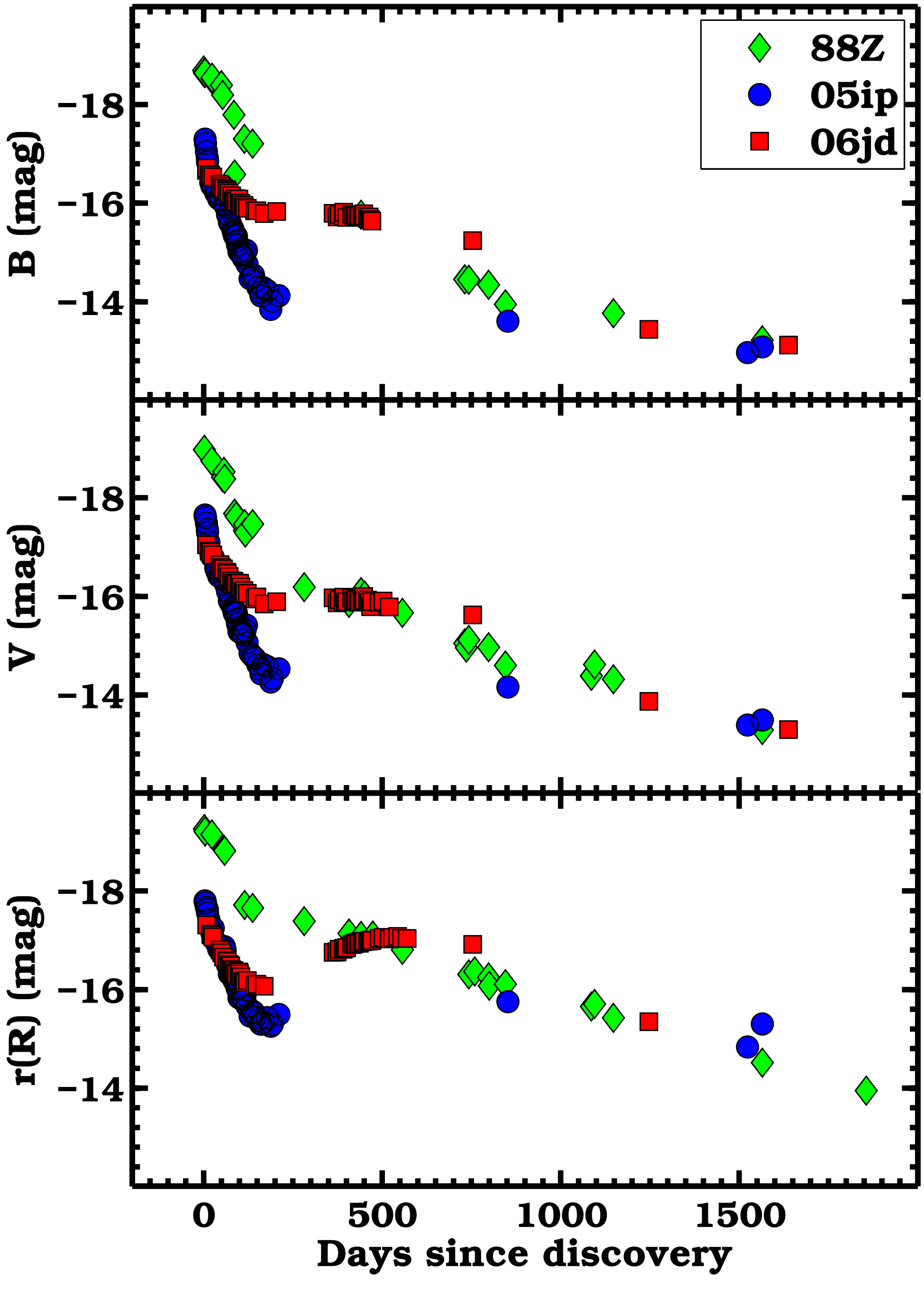

Fig. 17.— Comparison of absolute B-, V-, and r-band light curves of SNe 1988Z, 2005ip and 2006jd.

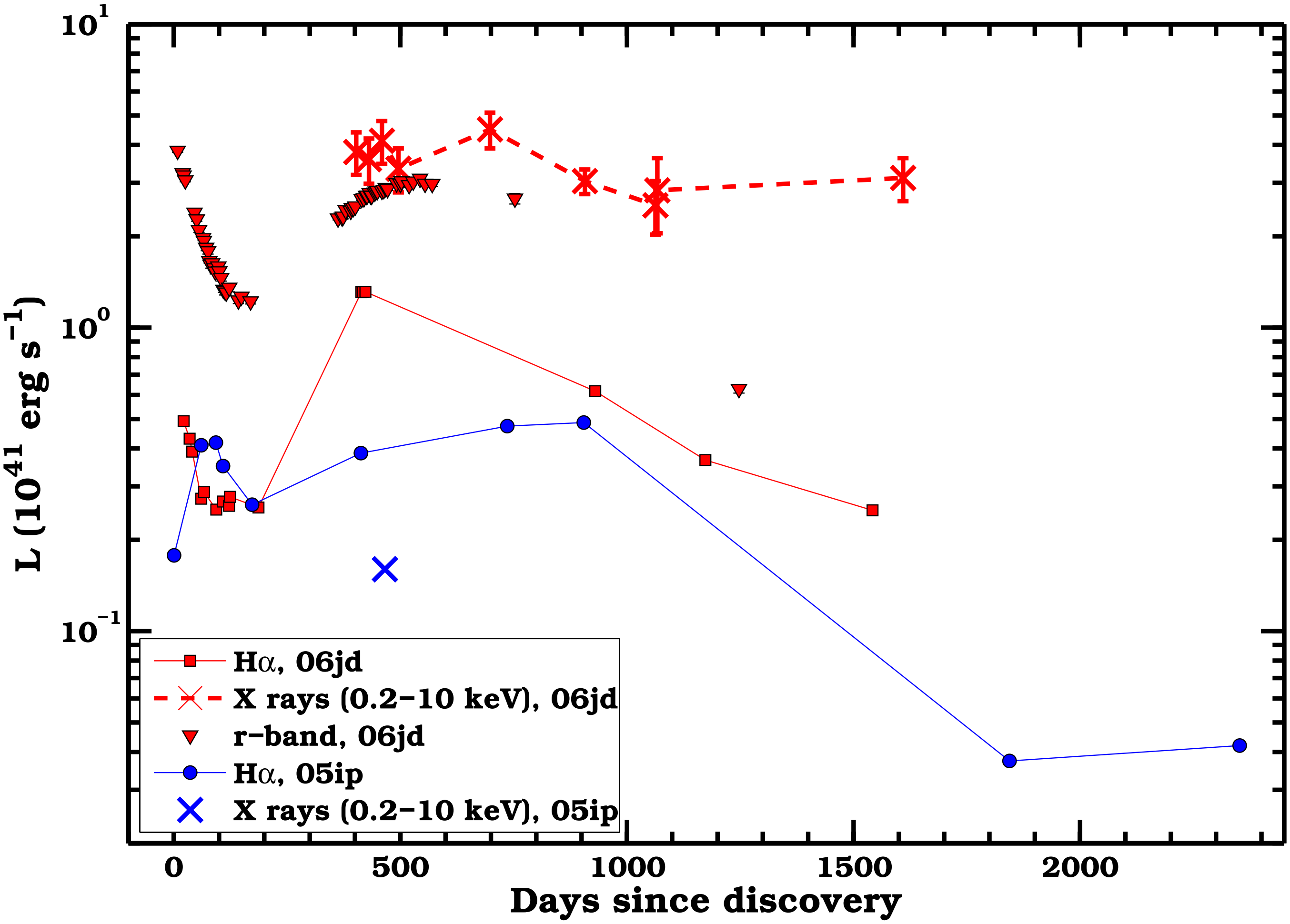

Fig. 18.— Comparison of Hα and reported X-ray luminosities of SNe 2005ip and 2006jd. Also included is the absolute *r*-band light curve of SN 2006jd.

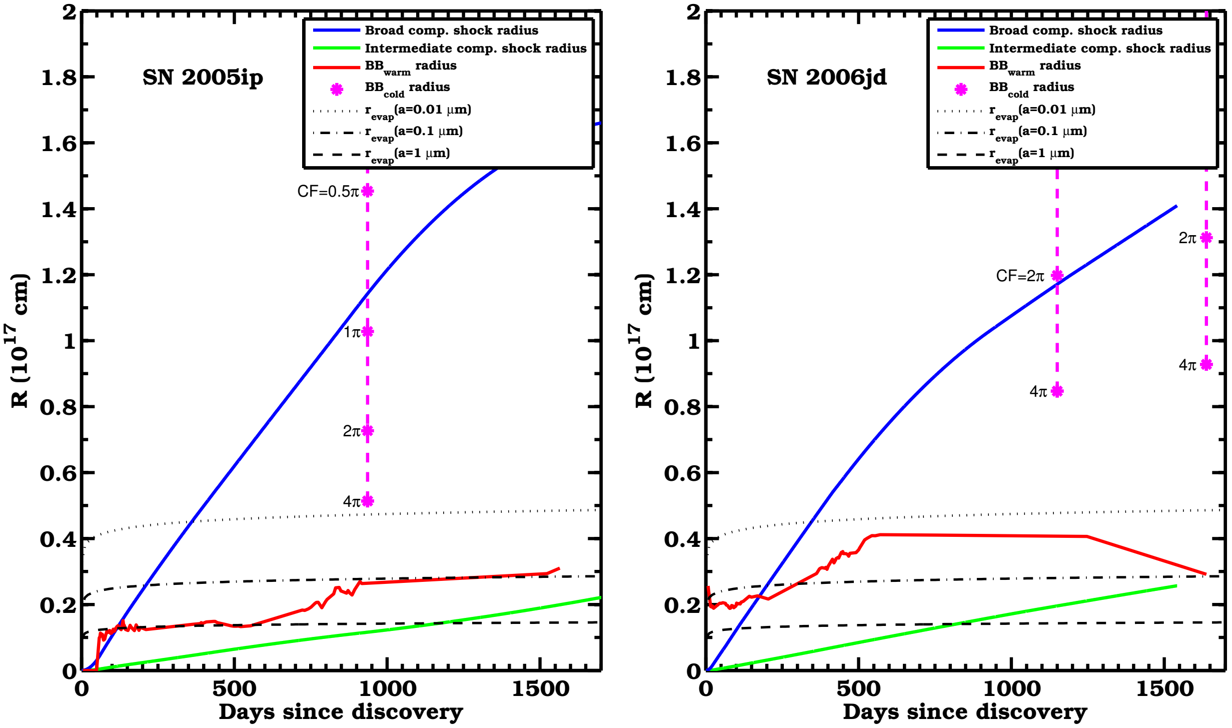

Fig. 19.— *BB* radii of the warm (red line) and cold (vertical, dot-dash line) dust components plotted as a function of days. The continuum of cold dust *BB* radii are indicated for various covering factors (CF). Also plotted are the locations of the fasting moving ejecta (blue line) and post-shocked gas (green line) estimated from the BVZI of the broad- and intermediate-width Hα emission profile. Horizontal dashed, dot-dashed, and doted lines are graphite dust evaporation radii for various grain sizes.